Summer Regional Climate Simulations Over Tibetan Plateau at Gray-Zone and Convection-Permitting Scale

Mengnan Ma
School of Atmospheric Sciences, Nanjing Unveisity
Tinghai Ou
Regional Climate Group, Department of Earth Sciences, University of Gothenburg
Dongqing Liu
Nanjing Meteorological Bureau
Shuyu Wang
School of Atmospheric Sciences, Nanjing University
Juan Fang
School of Atmospheric Sciences, Nanjing Univeristy
Jianping Tang (jptang@nju.edu.cn)
School of Atmospheric Sciences, Nanjing University https://orcid.org/0000-0002-1098-2656

Research Article

Keywords: Tibetan Plateau, gray zone, convection permitting, spectral nudging, summer precipitation, surface air temperature

Posted Date: October 19th, 2021

DOI: https://doi.org/10.21203/rs.3.rs-965944/v1

Abstract

The Tibetan Plateau (TP) is often referred to as ‘the Third Pole’ and plays an essential role in influencing the global climate. However, it remains challenging for most global and regional models to realistically simulate the characteristics of long-period climate over the TP. In this study, two Weather Research and Forecasting model (WRF) experiments using the regional climate simulation method of spectral nudging with gray-zone (GZ9) and convection-permitting (CP3) resolution are conducted for summer from 2009 to 2019. The surface air temperature (T2m) and precipitation are evaluated against in-situ observations and the Global Satellite Mapping of Precipitation (GSMaP) dataset. The results show that both experiments can successfully capture the spatial pattern and daily variation of T2m and precipitation, though cold bias for temperature and dry bias for precipitation exist especially over the regions south of 35ºN. Compared to GZ9, CP3 reduces the cold and dry bias over the southern TP. In addition, analysis of the diurnal variation of precipitation shows that both experiments simulate the advanced occurrence time of maximum precipitation by about 3 hours over the eastern TP but postpone the occurrence time of maximum precipitation over the central and western TP. Both experiments simulate a bimodal structure of the diurnal cycle of precipitation amount (PA). Further investigation reveals that GZ9 has more low-level clouds and prevents shortwave radiation from reaching the surface during daytime, leading to lower maximum surface air temperature (Tmax) in GZ9, while CP3 has more low-level clouds over the southeastern TP and preventing the outgoing longwave radiation and compensating the heat loss during nighttime, resulting in higher minimum surface air temperature (Tmin) in CP3. Besides, more water vapor over the southeastern TP results in more precipitation and thus reduced dry bias in CP3 over the southeastern TP. Moreover, the current study also indicates that gray-zone scale simulations can perform as good as convection-permitting simulations by carefully choosing the right parameterization schemes.

1. Introduction

The Tibetan Plateau (TP) extends over the area of 27°-45°N, 70°-105°E, covering a region about a quarter of the size of the Chinese territory (Wu et al. 2007). Surrounded by the Earth’s highest mountains, such as the Himalayas, Pamir, Kunlun Shan and others, it is the highest and most extensive plateau in the world (Kang et al. 2010; Xu et al. 2018; Gu et al. 2020) and has long been known as the roof of the world (Liu and Chen 2000; Qiu et al. 2008; Yao et al. 2019). Mountains in the TP have a strong impact on precipitation distribution, and a knowledge of the characteristics of precipitation is a basic and important requirement for the planning and management of water resources (Xu et al. 2008). Meanwhile, in the summer season, the TP serves as a huge heat source (Zhu et al. 2017), transferring heat from the land surface to the air in the form of sensible heating, latent heat transfer, and effective radiation of the ground (Yeh et al. 1957), with strong surface sensible heating and deep latent heating over the central and eastern regions (Duan et al. 2012), and plays an important role in the onset and maintenance of the Asian summer monsoon (Chen et al. 2017). However, precipitation across the Tibetan Plateau is poorly known compared with many other mountain areas in the world.

The complex climate over the TP is the key component of the regional and global climate system, but the lack of basic observation data makes it difficult to assess the impact that TP has on climate change across scales. Facing the fact that only sparse observation is available from heterogeneously distributed meteorological stations over the TP (Kuang and Jiao 2016; Maussion et al. 2011; Xiao et al. 2016; Li et al. 2018), numerical simulation results have been proven to be a reasonable and reliable complement to enhance the understanding of climate over the TP. Compared to the global climate models (GCMs), regional climate models (RCMs) are able to depict regional heterogeneity and leading to a better understanding of regional to local climate change signals. The main achievements in RCM research are benefited from the increase of simulation length and resolutions (Giorgi et al. 2019). Several studies have shown that added value is obtained by increasing the horizontal resolution of RCMs to capture additional fine-scale weather processes (Jacob et al. 2014; Di Luca et al. 2012; Lucas-Picher et al. 2012). With its complex orography, the TP is very sensitive to the horizontal resolution of RCMs (Gao et al. 2015a, b, 2017b). Gao et al. (2018) found that the WRF model with a resolution of about 30km shows reduced overestimation for extreme precipitation frequency, increased spatial pattern correlations, and more accurate linear trends compared with coarser resolution GCMs and reanalysis over the TP. Xu et al. (2018) showed that the added value of RCM simulation of about 25 km resolution is achieved by affecting the regional air circulation near the ground surface around the edge of the TP, which leads to a redistribution of the transport of atmospheric water vapor.

Convection is considered to be one of the most critical physical processes affecting the occurrence and amount of precipitation (Kukulies et al. 2020; Niu et al. 2020), while cumulus parameterization schemes (CPSs) have been considered to be a primary uncertainty source in precipitation simulations over the TP for coarse resolution (~25km) RCMs (Wang et al. 2021). Attempts have been made to solve the difficulty by further increasing the resolution of RCMs. The resolution between 10 and 4km is the so-called gray-zone at which resolution the individual convection cells cannot be resolved, but the organized mesoscale convective systems can be explicitly represented (Ou et al. 2020). With the gray-zone grid spacing, a CPS may or may not be turned on. In Asia, Chen et al. (2018) found that the WRF at the 9km gray-zone resolution without the use of CPS captures the salient features of the Indian summer monsoon as well as the spatial distributions and temporal evolutions of monsoon rainfall. Taraphdar et al. (2021) evaluated the WRF at the 9km gray-zone resolution over the United Arab Emirates (UAE) and the Middle-East, and found that gray-zone simulations' performance for the synoptic and meso-scale precipitation are comparable to convection-permitting simulations with optimized model physical packages. Ou et al. (2020), based on WRF simulations at gray-zone resolution with different CPSs and a simulation without CPS over the TP, found that the frequencies and initiation timings for short-duration (1–3 h) and long-duration (> 6 h) precipitation events are well captured by the experiment without CPS concerning the precipitation diurnal cycles.

Future directions in RCM research are discussed by Giorgi et al. (2019), with a highlight on the transition to convection-permitting modeling systems. Benefited from the rapid development of high-performance computing resources, convection-permitting models (CPMs) is becoming affordable for climate study, which could explicitly resolve the deep convection (Liang et al. 2004; Dai 2006; Prein et al. 2015; Zhang

and Chen 2016), eliminate the biases resulted from the application of CPSs, and narrow the uncertainty from model physics (Weisman et al. 1997; Miura 2007; Schlemmer et al. 2011; Satoh et al. 2014; Ban et al. 2015), especially over regions with prevailing convective activities. Many studies have demonstrated the benefits of using CPMs, including the ability to capture observed precipitation diurnal cycles over subtropics (Fosser et al. 2015; Guo et al. 2019, 2020; Li et al. 2020; Yun et al. 2020), well replicating the spatial distribution of precipitation over complex terrain (Grell et al. 2000; Prein et al. 2013; Rasmussen et al. 2014; Gao et al. 2020), and even capable of representing the spatial-temporal scales and the organization of tropical convection at the nearly global scale (Schiwitalla et al. 2020). Zhou et al. (2021) found that CPM outperforms the High Asia Refined regional reanalysis (HAR v2, Maussion et al. 2011) for 10-m wind speed and precipitation with obviously reduced wet bias over the TP. Lin et al. (2018) showed that the WRF with 2km grid spacing can diminish the positive precipitation bias over the TP and better resolve the orographic drag as well as mountain-valley circulations. Li et al. (2021) demonstrated that CPM is a promising tool for dynamic downscaling over the TP with its higher ability to depict the precipitation frequency and intensity and Lv et al. (2020) found that the choice of the land surface model (LSM) scheme in CPM also has a certain influence on the precipitation's spatial pattern, frequency, diurnal cycle, and intensity over the central TP.

Both gray-zone and CPM simulations are at their earlier stages in regional climate application. Though intercomparison of the two types of high-resolution simulations has been performed during the past years, few studies have focused on the TP. Furthermore, previous studies with CPM over the TP were mostly limited to short-term simulation. In this study, two types of high-resolution experiments using the WRF model, the gray-zone resolution of 9km with no CPS and the convection-permitting (CP) resolution of 3km, are performed over the TP for the summer of 2009 to 2019. By comparing the two sets of simulation results, we can: (1) evaluate the model’s performance with various resolutions in reproducing the spatiotemporal characteristics of surface climate over the TP; (2) identify the added value of convection-permitting simulation over complex terrain and climate system; and (3) isolate the contribution of the convection-permitting experiments in improving the simulation of regional climate processes.

The article is organized as follows. Section 2 describes the model and experimental design, data and methodology. Section 3 presents the main results as well as the comparison with the observations, including the added value of CPM simulation. Section 4 discusses the possible reasons for explaining the excessive precipitation and higher 2-m air temperature in CPM simulation. Finally, major conclusions are presented in Section 5.

2. Model, Experimental Design And Data

2.1 Model and experimental design

The WRF model version 4.1.1 (Skamarock et al. 2019) used in this study is a nonhydrostatic mesoscale numerical weather prediction system, which is designed to serve both operational forecasting and

atmospheric research needs. The WRF model has been widely used for CPM regional climate simulations over Europe (Warrach-Sagi et al. 2013), North America (Gao et al. 2017a; Liu et al. 2017; Sun et al. 2016), Eastern China (Guo et al. 2019, 2020; Yun et al. 2020) and over the TP (Zhou et al. 2021; Gao et al. 2020). The simulation domain in this study is centered at 33°N and 88.5°E, with 1081 (361) grid points in east-west directions and 721 (241) grid points in north-south directions for 3km (9km) resolution, covering the whole TP and the surrounding areas (Figure 1a). Four sub-regions are chosen based on the topography and climate features to evaluate the skill of WRF in reproducing the regional climate over the TP in detail: the northwest region (TP-NW, 32.5°–37°N, 75°–91°E), the southwest region (TP-SW, 28°–32.5°N, 82°–91°E), the northeast region (TP-NE, 32.5°–39°N, 91°–102°E) and the southeast region (TP-SE, 28°–32.5°N, 91°–102°E). Fifty hybrid-sigma levels are defined from surface to model top at 50hPa. The horizontal resolution is set to 9 km for the gray-zone scale simulation (GZ9) and 3 km for the CP scale simulation (CP3) over the TP.

The physical parameterization schemes employed in this research include the Thompson microphysics scheme (Thompson et al. 2008), the Mellor-Yamada Nakanishi Niino 2.5 level TKE scheme (MYNN) planetary boundary layer (PBL) parameterization (Nakanishi and Niino 2006), the RRTMG shortwave and longwave radiation schemes (Iacono et al. 2008), and the Noah-MP land surface model (Niu et al. 2011). In the two experiments, the CPS is switched off.

Spectral nudging (hereinafter SN, von Storch et al. 2000), which is mostly used in models driven by global analysis (Tang et al. 2010, 2017), has been adopted in CP3 and GZ9. In this study, the nudging wavenumber of 4 is employed in both directions and the nudging coefficient is $3X10\text{-}4$. Meanwhile, the SN approach is only applied to wind fields above the PBL to allow the development of the mesoscale circulation.

All the experiments are driven by the 4th generation Global Reanalysis data (ERA5) from Europe Centre for Medium-Range Weather Forecasts (ECMWF) (Hersbach et al. 2020) and conducted during the summer season (June, July, and August) from 2009 to 2019. The simulation starts from May 16 and integrates continuously to September 1, with the first 16 days (May 16-31) as the spin-up time.

2.2 Observation data and method

To evaluate the performance of the WRF model in simulating the surface climate over the TP, two observation datasets are used. One is the daily in-situ observation provided by the data service center at China Meteorology Administration (CMA, http://data.cma.cn/en). Only 144 stations over the TP are applied in this study (Figure 1b), which have comparatively more applicable observations of daily surface air temperature (T2m), maximum/minimum surface air temperature (Tmax and Tmin), and precipitation. Most of the meteorological stations are located in the central and eastern part of the TP while few of them are located over the western TP. Therefore, the data from the meteorological stations are not sufficient to fully depict the climate characteristics over the whole TP, especially over the western TP and regions above 4,800 ASL. This is especially true for precipitation which has relatively small spatial scales

over the TP (Chen et al. 2016). Thus, to validate the WRF-simulated precipitation over the TP in detail, satellite precipitation products are also used to carry out a more objective and comprehensive evaluation.

The Global Satellite Mapping of Precipitation version 6 (GSMaP) products, operated by the Japan Aerospace Exploration Agency (JAXA), are used in this study. GSMaP combines precipitation retrievals from the Tropical Rainfall Measuring Mission and other polar-orbiting satellites and interpolates them with cloud motion vectors derived from infrared images from geostationary satellites to produce a high-resolution dataset (Tian et al. 2010). The spatiotemporal resolution of the GSMaP products is 0.1° x 0.1° and 1-hour. The gauge-adjusted GSMaP data (GSMaP-Gauge) is adopted to evaluate the WRF simulation, which is a gauge-calibrated product by adjusting the GSMaP estimate using the National Oceanic and Atmospheric Administration (NOAA)/Climate Prediction Center (CPC) gauge-based analysis of global daily precipitation. GSMaP, which covers the whole TP with a considerably high resolution, can provide a more objective evaluation, especially over the western TP. Ning et al. (2017) found that at basin scale comparisons, the GSMap-gauged data has relatively higher accuracy than IMERG, especially at the Haihe, Huaihe, Liaohe, and Yellow River basins. Lu and Yong (2018) pointed out that GSMaP-Gauge demonstrated comparable performance with gauge reference data, suggesting that GSMaP-Gauge can be selected for hydrological application over the TP.

Several statistics are calculated to quantify the accuracy of the WRF simulations, including the correlation coefficient, the uncentered root-mean-square error (RMSE), and the relative bias (RB). The correlation coefficient is used to describe the temporal and spatial similarity between the observations and the simulations. The RMSE can measure the average magnitude of the deviation of a model simulation from the observation, with mean error, correlation coefficient, and standard deviation considered (Taylor et al. 2001).

3. Results From Wrf Simulations At Gray-zone And Convection-permitting Scale

Evaluation of the WRF experiments (CP3 and GZ9) is mainly for the surface climate of T2m, Tmax, Tmin, and precipitation, as well as the diurnal variation of precipitation over the TP. In order to compare with the in-situ observations and the satellite precipitation products, the WRF simulation results were interpolated onto the stations when compared with in-situ observations as well as the grid cells of the GSMaP dataset when compared with the satellite precipitation products, using the inverse distance weight interpolation method. Due to the elevation difference between WRF grids and station location, lapse rate (LR) is used to bias correct the WRF simulated surface air temperature when evaluation the WRF outputs against in-situ observations. According to the spatiotemporal variability of LR proposed by Wang et al. (2018), the mean LRs over the western TP, northeastern TP, and southeastern TP during summer are −4.90, −4.53, and −4.03 K/km, respectively, which are consistently lower than the commonly used global mean LR (−6.5 K/km) and are used for bias correction in this study.

3.1 Summer mean surface air temperature and precipitation

Figure 2 shows the 11-year averaged (2009-2019) summer mean daily T2m, Tmax, and Tmin from the in-situ observations, and the differences between the WRF simulations and the observations. The observed T2m decreases from the southeastern TP to the northwestern TP, with the maximum T2m at about 22℃ over the eastern TP while the minimum T2m below 8℃ over the central TP. Both the WRF experiments can well reproduce the spatial pattern of T2m with the spatial correlation coefficients (SCCs) larger than 0.94, but underestimate the T2m over the regions south of 35°N. Compared to GZ9, CP3 clearly improve the surface air temperature simulation with lower biases. The simulated distributions of Tmax and Tmin also agree well with the observations, with the SCCs above 0.90 and the RMSEs below 2.7℃. Overall, CP3 tends to simulate higher surface air temperature than GZ9 over the TP, and thus shows more skillful performance in reproducing the spatial patterns of T2m, Tmax, and Tmin with reduced RMSEs and higher SCCs, especially over the southern TP. The daily temperature range (DTR) is higher over the regions north of 30°N according to the station observations, exceeding 13℃ (figure not shown), while the minimum DTR below 10°C is detected over the southeastern TP. All the WRF experiments can well simulate the spatial pattern of DTR with the SCCs higher than 0.75 and the RMSEs less than 1.5℃. However, obvious clod bias exists over the southern TP. Moreover, CP3 can reduce the RMSE by about 0.8°C over the southeastern TP compared with GZ9.

Figure 3 shows the 11-year averaged summer mean precipitation from the station observations, the GSMaP satellite dataset, and the differences between the WRF simulations and the observations. The observed precipitation decreases from southeast to northwest, with the maximum above 6mm/day located at the southeastern corner of TP and the minimum less than 1mm/day over the northeast TP. Both CP3 and GZ9 can well capture the spatial distribution of summer mean precipitation, with SCCs larger than 0.72 and RMSEs below 1.1 mm/day compared with the station observations. However, the WRF model clearly underestimates summer precipitation over most regions of TP, especially over the southern TP. When compared against the GSMaP precipitation dataset, WRF simulations underestimate summer precipitation over southeastern TP and overestimate it over northwestern TP. Both CP3 and GZ9 have similar SCCs above 0.7 and relatively large RMSEs greater than 2mm/day. Comparison with both observational datasets shows consistency over the southeastern TP where both WRF simulations demonstrate dry bias. However, in most regions over the northwestern TP without the station observations, results show that GZ9 has a larger wet bias than CP3 based on the comparison against the GSMaP dataset. Thus, it may be deduced that by increasing the horizontal resolution, the dry (wet) bias over the southeastern (northwestern) TP can be reduced. In general, both experiments can reproduce the distribution of summer mean precipitation over TP and show consistent dry bias over southeastern TP and wet bias over northwestern TP. With higher horizontal resolution than GZ9, CP3 tends to improve the precipitation simulation by producing more precipitation over southeastern TP and less precipitation over the northwestern TP.

The Taylor diagrams are presented to evaluate the two WRF experiments in simulating the spatial distributions of summer temperature and precipitation (Figure 4) over the TP for each year (2009-2019). GZ9 and CP3 have similar performances in simulation the distributions of T2m, Tmax, and Tmin with the SCCs larger than 0.95. CP3 slightly improved performance with higher SCC and closer distance to

observations (REF point) than GZ9. For the precipitation, the two WRF experiments also show comparable performances when compared with the station observations. However, CP3 outperforms GZ9 with higher SCCs (> 0.7) when the GSMaP precipitation dataset is used as a reference. In general, both experiments exhibit comparable ability in reproducing the spatial pattern of summer mean surface air temperature and precipitation during 2009-2019, with reasonable cold bias and dry bias, especially over the regions south of 35°N.

3.2 Daily surface temperature and precipitation

The 11-year averaged (2009-2019) daily variations of the regional mean (over the TP) T2m, Tmax, Tmin, and DTR from the in-situ observations and WRF experiments are shown in Figure 5. The observed T2m ranges from 12℃ to 16℃ throughout the summertime, with the maximum T2m in early and middle July. All the WRF experiments can well capture the daily variation of T2m with the temporal correlation coefficients (TCCs) higher than 0.95 and the RMSEs less than 1.1℃. CP3 outperforms GZ9 by reducing the cold bias. The Tmax ranges from 18℃ to 24℃ based on the observation, and CP3 and GZ9 also well simulate the daily variation with the cold bias of about 1.0℃ for CP3 and 2.0℃ for GZ9. For Tmin, CP3 can also reduce the RMSE by about 0.6℃ compared to GZ9. The observed DTR varies between 9℃ and 15℃, with the minimum DTR occurring in early July. Both WRF experiments reproduce the daily DTR variation with the TCCs larger than 0.91 and the RMSEs less than 1.2℃, and colder bias occurs in late July and early August. CP3 tends to simulate the DTR closer to observation. Both WRF experiments show comparable performance in reproducing the daily variation of surface air temperature and DTR, but underestimation is obviously reduced in CP3, especially for Tmax with the most significant reduction at about 1℃.

Regarding the daily variation of regional mean precipitation over the TP (Figure 6), both CP3 and GZ9 can reproduce the daily variation with the TCCs all above 0.9 and the RMSEs below 0.75 mm/day when compared with the station observations. Compared with in-situ observation, both experiments can better simulate the precipitation with negligible bias in early and middle June but growing dry bias since early July. While the two experiments obviously overestimate the daily precipitation when selecting the GSMap as the reference, with wetter bias in GZ9 has and a larger RMSE of about 0.92 mm/day than CP3. Whether station observation or GSMaP dataset is selected as reference, both WRF experiments consistently have TCCs above 0.9 and RMSEs below 1mm/day.

The spatial distributions of TCCs and RMSEs of T2m, Tmax, and Tmin at each observation station are shown in Figure 7 and Figure 8, respectively. The spatial patterns of TCCs of T2m and Tmax are quite similar in both CP3 and GZ9, with high TCCs above 0.9 are located over the northeastern TP and decrease from north to south. Compared with GZ9, CP3 exhibits higher TCCs of T2m and Tmax, especially over the southern TP. The WRF model has relatively lower performance in simulating variation of Tmin than that of T2m, with the TCCs ranging from 0.5 to 0.8. GZ9 shows higher TCCs for Tmin compared with CP3. For RMSEs, both experiments show large RMSEs (above 3.0℃) for Tmax over the southern TP and for Tmin over the northern TP, while CP3 demonstrates smaller RMSE for T2m compared to GZ9. CP3 can also reduce RMSE for Tmax and Tmin over the southern TP, especially for Tmax with the

maximum reduction at about 1.6℃. Therefore, it can be concluded that CP3 improves the simulation of T2m and Tmax with higher TCCs and lower RMSEs, especially over the southern TP.

The spatial distribution of TCC and RMSE of the simulated daily precipitation for WRF experiments against station observation is presented in Figure 9. The two experiments show quite similar spatial patterns of TCC and RMSE. High TCCs exist over eastern TP and low RMSEs are located over central and northern TP. CP3 has slightly increased the TCCs by about 0.1 and reduced the RMSEs by about 0.5 mm/day over the southeastern TP, which is also validated by the comparison against GSMaP (figure not shown).

In general, both CP3 and GZ9 show comparable performance in reproducing the daily variation of surface air temperature, and CP3 obviously improves the performance by reducing the cold biases. Meanwhile, CP3 improves the ability to reproduce T2m and Tmax with higher TCCs and lower RMSEs compared to GZ9, especially over the southern TP. For precipitation, both experiments can well reproduce the spatiotemporal characteristics, while CP3 shows better skills with slightly increased TCC and reduced RMSE over the southeastern TP.

3.3 Diurnal cycle of precipitation

To evaluate the performance of WRF in simulating the diurnal variation of summer precipitation over the whole TP, the GSMaP satellite precipitation dataset is selected as the reference. The precipitation frequency (PF) is defined as the percentage of all hours during the period which had measurable precipitation (> 0.1 mm/h), the precipitation intensity (PI) is defined as the average precipitation rate over all the precipitating hours, and the precipitation amount (PA) is defined as the accumulated precipitation amount over a given time period.

The 11-year averaged (2009-2019) occurrence time of maximum PA and PF in a day from the observation and WRF experiments is presented in Figure 10. The observed maximum PA and PF mostly occurs after 18:00 Local Standard Time (LST) over the TP, with the latest occurrence time of maximum PA after 22:00 LST located over the southeastern TP. All the WRF experiments can capture the spatial pattern of the occurrence time of maximum PA, with about 3 hours in advance over the eastern TP. However, over the central and western TP, both experiments simulate a postponed occurrence time of maximum PA of about 2 hours.

Figure 11 shows the 11-year averaged regional mean diurnal cycle of PA and PI over the whole TP and four subregions (TP-NW, TP-SW, TP-NE, and TP-SE). It can be found that the observed PA ranges from 0.05 to 0.2 mm/hour over the TP, with two peaks occurring at 17:00 LST and 22:00 LST. Both CP3 and GZ9 can reproduce the bimodal structure of the diurnal variation of PA over the TP, but they all have delayed the peak at 22:00 LST by 3 hours. GZ9 can successfully capture the afternoon precipitation peak while CP3 slightly simulates the peak by 1 hour earlier. Compared with GZ9, CP3 shows reduced wet bias, especially from late afternoon to night. The diurnal variations of PF are similar to those of PA (figure not shown) with obvious nocturnal precipitation. Both GZ9 and CP3 can capture the diurnal variation of PI

with consistent overestimation, which may contribute to the overestimation of PA. Both experiments can well capture the characteristics of the diurnal cycle of PA over TP-NW but with stronger amplitudes, where the RB is about 117.1% in CP3 and 148.8% in GZ9 respectively. The WRF experiments show the most skillful performance in simulating the diurnal variation over TP-NE with the most reduced wet bias. Over TP-SE and TP-SW, the observed diurnal variations of PA are quite similar, with peaks occurring in the afternoon and night. Both experiments can generally reproduce the diurnal variation with obvious dry bias at nighttime.

In general, WRF experiments tend to simulate much stronger afternoon precipitation over the eastern TP, which is ahead of observation, while simulating stronger nighttime precipitation over the western TP, which is behind the observation. CP3 can reduce wet bias over the northern TP, while it shows little superiority in reducing the dry bias at nighttime over the southern TP. Again, as a satellite-derived product, GSMaP needs to be calibrated with station observations. However, there are only fewer station sites located over the central and western TP. Currently, the uncertainty in this satellite-derived dataset is hard to be avoided. With more observations and reduced uncertainty in precipitation datasets, a better understanding can be got.

4. Discussion

4.1 Surface energy balance

To investigate the causes of the reduced cold biases in CP3 over TP, the 11-year averaged surface energy balance is studied. According to Xu et al. (2015), the surface energy balance equation is as follows:

$$\sigma T_s^4 = SW\downarrow - SW\uparrow + LW\downarrow - (SH + LH + GHF), \quad (1)$$

where σ, T_s, $SW\downarrow$, $SW\uparrow$, $LW\downarrow$, SH, LH and GHF represent the Stefan-Boltzmann constant, skin temperature, downward shortwave radiation, upward shortwave radiation, downward longwave radiation, sensible heat flux, latent heat flux and ground heat flux, respectively. The sum of the net shortwave radiation and downward longwave radiation (received radiative energy is represented with positive values), the sum of heat loss in the form of sensible and latent heat flux and ground heat flux (non-radiative energy loss is represented with positive values), as well as the sum of the right-hand terms (net energy obtained is represented with positive values) at 06:00 and 18:00 UTC from the WRF experiments are plotted in Figure 12 and Figure 13, which could reflect the spatial pattern of skin temperature and further to surface air temperature.

It can be found that the received radiative energy in CP3 is about 40-50 larger than that of GZ9 over most regions of the TP at 14:00 LST (Figure 12a-c), which is mainly contributed by stronger downward shortwave radiation (figure not shown) in CP3. Meanwhile, the non-radiative energy loss is also larger in

CP3 than that of GZ9 (Figure 12f), which is mainly caused by the stronger upward sensible and latent heat fluxes in CP3 (figure not shown). There also exists more heat flux transported from the surface to the deeper soil in CP3 than GZ9 (figure not shown) over the central and southeastern TP. As a result, large non-radiative heat fluxes loss in the form of sensible and latent heat fluxes and ground heat fluxes is compensated by the received radiative energy, leading to more energy storage on the surface over the TP in CP3 (Figure 12i) and higher skin temperature, and then further leads to the warmer daily maximum surface air temperature.

At nighttime (02:00 LST), over the central and western TP, although CP3 produces less downward longwave radiation (Figure 13c), there is non-radiative energy compensation in the form of downward non-radiative heat fluxes and upward ground heat flux in CP3 (Figure 13f). As a result, it simulates higher skin temperature and further leads to higher surface air temperature at night (Tmin) over the central and western TP. Meanwhile, over the eastern TP and along the south slope of TP, both larger downward longwave radiation and larger non-radiative energy loss co-exist in CP3 than GZ9. However, the larger downward longwave radiation in CP3 than GZ9 makes up for the heat loss and leads to more energy storage on the surface in CP3 which further leads to higher surface air temperature at night (Tmin) over the eastern TP and along the south slope of TP. Therefore, although the energy storage on the surface comes from different ways in CP3, which is mainly from non-radiative energy over the central and western TP and radiative energy over the eastern TP. It finally similarly results in the higher Tmin over most regions over the TP.

4.2 Low-level meteorological elements distribution

The surface energy balance results show that the received radiative energy, mainly from shortwave radiation, at 14:00 LST contributes the most to the conserved energy in CP3. Therefore, the low-level cloud fraction, which plays the most important role in modulating the solar radiation reaching the surface, is studied to reveal the causing factors to the more downward shortwave radiation in CP3. The 11-year averaged cloud fraction at 02:00 and 14:00 LST are shown in Figure 14. The cloud fraction of 02:00 and 14:00 LST at 500hPa has a similar spatial pattern in both experiments. At daytime (14:00 LST), more clouds occur over the eastern TP with the maximum value of cloud fraction above 50% over the southeastern TP; fewer clouds occur over the western and central TP with cloud fraction below 5%. GZ9 simulates more clouds over most regions of the TP than CP3, in which the low-level clouds reflect more shortwave radiation to space. This then results in less energy conserved and lower maximum surface air temperature in a day. Similarly, at nighttime (02:00 LST), the cloud fraction at 500hPa decreases from the southeastern TP to the northwestern TP in both experiments. CP3 tends to simulate more clouds than GZ9 over the eastern TP and along the southern slope of TP, which has a similar spatial pattern with downward longwave radiation in Figure 13. More clouds over these regions in CP3 can warm up the low boundary layer through downward longwave radiation at night. In addition, more water vapor, which is crucial for the formation of low-level clouds, is also found (figure not shown) where the clouds are dense. Therefore, clouds at low-level over the TP play an important role in regulating the radiation that can reach the surface and further influence the surface air temperature through energy balance.

Available atmospheric water vapor is very important for precipitation. Figure 15 shows the 11-year averaged water vapor mixing ratio at low-level (500hPa) over the TP in the two WRF experiments. In both experiments, water vapor decreases from the southeastern TP to the northwest, with the spatial distribution pattern similar to that of precipitation simulated. In CP3, more water vapor exists over the southeastern TP, which may be related to stronger moisture convergence transporting abundant water vapor, and partly contributes to more precipitation than GZ9. Meanwhile, over the northwestern TP, more water vapor is found in GZ9 which also partly leads to more severe wet bias than CP3. Therefore, more precipitation generated in CP3 over the southeastern TP as well as more precipitation in GZ9 over the northwestern TP can be well explained with the more atmospheric water vapor.

5. Conclusions

Two WRF experiments with the regional climate simulation schemes of spectral nudging at gray-zone and convection-permitting resolution are performed over the TP from 2009 to 2019. The surface air temperature and the precipitation are evaluated based on the in-situ observations and the GSMaP dataset.

Both WRF experiments successfully capture the spatial patterns and the daily variation of T2m, Tmax, and Tmin, with the SCCs and TCCs higher than 0.9. A generally cold bias is found, especially over the regions south of 35°N for T2m. CP3 shows more skillful performance in reducing the RMSEs over the southern TP for T2m, Tmax, and Tmin. Meanwhile, CP3 has improved TCCs and reduced RMSEs over the southern TP for T2m and Tmax. The DTR is underestimated by about 1℃ spatially and temporally in both experiments, with reduced cold bias especially over the southeastern TP in CP3. Further analysis of multi-year averaged surface energy budget and low-level cloud fraction reveals that GZ9 has more low-level clouds during daytime over the TP, reflecting more shortwave radiation to space, leading to less downward shortwave radiation and lower Tmax than those of CP3. On the contrary, CP3 produces more low-level clouds especially over the eastern TP and along the south slope of TP at nighttime, preventing the outgoing longwave radiation and compensating the heat loss, and increasing the Tmin consequently. Meanwhile, the more non-radiative heat fluxes over the central and western TP contribute a lot to the higher Tmin in CP3. As a result, the simulation of DTR and T2m in CP3 is further improved due to the better depiction of Tmax and Tmin.

The spatial pattern and daily variation of summer precipitation are also reasonably reproduced in both WRF experiments, with the SCCs larger than 0.7 and the TCCs larger than 0.9. Dry bias is found over the regions south of 35°N compared with both station observation and the GSMaP dataset. CP3 tends to simulate more precipitation and reduce the dry bias in most regions over the southeastern TP. However, GZ9 shows wetter bias over the northwestern TP than CP3. Both experiments underestimate the daily variation of precipitation when compared with station observations while overestimating that when compared with the GSMaP dataset, indicating the uncertainty coming from different sources of observation especially over complex terrains such as TP. The spatial distribution of water vapor mixing ratio at 500hPa matches well with that of precipitation and well explains more precipitation in CP3 than

GZ9 over the southeastern TP and wetter bias in GZ9 over the northwestern TP. To get a more in depth understanding of the temporal variation of summer precipitation over the TP, the diurnal cycle of precipitation is studied. Both experiments simulate a more advanced occurrence time of maximum precipitation in a day by about 3 hours over the southeastern TP while postponing the occurrence time by about 2hours over the western TP. In addition, the bimodal structure of PA is well captured and GZ9 successfully reproduces the peak in theafternoon which is postponed by 1 hour in CP3. However, wet bias is reduced in CP3 from late afternoon to night. Meanwhile, PF is also reasonably simulated in WRF simulations with obvious nocturnal precipitation. Moreover, PI is overestimated over the TP, indicating that the overestimation of PA in both experiments may be induced by the overestimation of PI.

Based on the analysis of surface air temperature and precipitation over the TP from 2009 to 2019, WRF experiments at gray-zone and convection-permitting scales show comparable performance in successfully reproducing the spatial and temporal variation of multi-year climate. A higher horizontal resolution, therefore, has complex effects on the results of simulations. For example, our results show that even though CP3 can slightly reduce the RMSEs for temperature and precipitation, GZ9 outperforms CP3 in capturing the peaks of PA over the TP. In addition, for the purpose of saving computation costs, experiments with gray-zone resolution are also a better choice especially for simulating long-period climate over the TP. Future studies in this area should include further looking for more advantages in experiments with convection-permitting resolution and make more improvements to experiments with gray-zone resolution and make them better utilized in the field of climate studies.

Declarations

Acknowledgments:

The research is supported by the Second Tibetan Plateau Scientific Expedition and Research Program (STEP, Grant No.2019QZKK0206), National Key Research and Development Program of China (2018YFA0606003) and the National Natural Science Foundation of China (41875124) as well as the Swedish Foundation for International Cooperation in Research and Higher Education (CH2019-8377).

Authors' contributions:

All authors contributed to the study conception and design. Material preparation, data collection and analysis were performed by Mengnan Ma, Dongqing Liu and Juan Fang. Tinghai Ou, Shuyu Wang and Jianping Tang helped perform the analysis with constructive discussions. The first draft of the manuscript was written by Mengnan Ma and all authors commented on previous versions of the manuscript. All authors read and approved the final manuscript.

Funding:

This work was supported by the Second Tibetan Plateau Scientific Expedition and Research Program (STEP, Grant No.2019QZKK0206), National Key Research and Development Program of China

(2018YFA0606003) and the National Natural Science Foundation of China (41875124) as well as the Swedish Foundation for International Cooperation in Research and Higher Education (CH2019-8377).

Availability of data and material

The station observations used in this work are available at: http://data.cma.cn/en.

The GSMap satellite dataset is available at: https://sharaku.eorc.jaxa.jp/GSMaP/

Code availability

The analysis code is available on request from the corresponding author.

1. Conflicts of interest

The authors have no conflicts of interest to declare that are relevant to the content of this article.

2. Consent to participate

Written informed consent was obtained from all participants.

3. Consent for publication

Written informed consent for publication was obtained from all participants.

References

1. Ban, N., Schmidli, J., & Schär, C. (2015). Heavy precipitation in a changing climate: Does short-term summer precipitation increase faster? *Geophysical Research Letters, 42*(4), 1165-1172. https://doi.org/10.1002/2014gl062588
2. Chen, D., Tian, Y., Yao, T., & Ou, T. (2016, Aug 24). Satellite measurements reveal strong anisotropy in spatial coherence of climate variations over the Tibet Plateau. *Sci Rep, 6*, 30304. https://doi.org/10.1038/srep30304
3. Chen, X., Liu, Y., & Wu, G. (2017). Understanding the surface temperature cold bias in CMIP5 AGCMs over the Tibetan Plateau. *Advances in Atmospheric Sciences, 34*(12), 1447-1460. https://doi.org/10.1007s00376-017-6326-9
4. Chen, X., Pauluis, O. M., & Zhang, F. (2018). Regional simulation of Indian summer monsoon intraseasonal oscillations at gray-zone resolution. *Atmospheric Chemistry and Physics, 18*(2), 1003-1022. https://doi.org/10.5194/acp-18-1003-2018
5. Dai, A. (2006). Precipitation characteristics in eighteen coupled climate models. *Journal of Climate, 19*(18), 4605-4630. https://doi.org/10.1175/JCLI3884.1
6. Di Luca, A., de Elía, R., & Laprise, R. (2011). Potential for added value in precipitation simulated by high-resolution nested Regional Climate Models and observations. *Climate Dynamics, 38*(5-6), 1229-

1247. https://doi.org/10.1007/s00382-011-1068-3

7. Duan, A., Wu, G., Liu, Y., Ma, Y., & Zhao, P. (2012). Weather and climate effects of the Tibetan Plateau. *Advances in Atmospheric Sciences, 29*(5), 978-992. https://doi.org/10.1007/s00376-012-1220-y
8. Fosser, G., Khodayar, S., & Berg, P. (2015). Benefit of convection permitting climate model simulations in the representation of convective precipitation. *Climate Dynamics, 44*(1-2), 45-60. https://doi.org/10.1007/s00382-014-2242-1
9. Gao, Y., Chen, F., & Jiang, Y. (2020). Evaluation of a Convection-Permitting Modeling of Precipitation over the Tibetan Plateau and Its Influences on the Simulation of Snow-Cover Fraction. *Journal of Hydrometeorology, 21*(7), 1531-1548. https://doi.org/10.1175/jhm-d-19-0277.1
10. Gao, Y., Leung, L. R., Zhang, Y., & Cuo, L. (2015). Changes in Moisture Flux over the Tibetan Plateau during 1979–2011: Insights from a High-Resolution Simulation. *Journal of Climate, 28*(10), 4185-4197. https://doi.org/10.1175/jcli-d-14-00581.1
11. Gao, Y., Leung, L. R., Zhao, C., & Hagos, S. (2017). Sensitivity of U.S. summer precipitation to model resolution and convective parameterizations across gray zone resolutions. *Journal of Geophysical Research: Atmospheres, 122*(5), 2714-2733. https://doi.org/10.1002/2016jd025896
12. Gao, Y., Xiao, L., Chen, D., Chen, F., Xu, J., & Xu, Y. (2017). Quantification of the relative role of land-surface processes and large-scale forcing in dynamic downscaling over the Tibetan Plateau. *Climate Dynamics, 48*(5-6), 1705-1721. https://doi.org/10.1007/s00382-016-3168-6
13. Gao, Y., Xiao, L., Chen, D., Xu, J., & Zhang, H. (2018). Comparison between past and future extreme precipitations simulated by global and regional climate models over the Tibetan Plateau. *International Journal of Climatology, 38*(3), 1285-1297. https://doi.org/10.1002/joc.5243
14. Gao, Y., Xu, J., & Chen, D. (2015). Evaluation of WRF mesoscale climate simulations over the Tibetan Plateau during 1979–2011. *Journal of Climate, 28*(7), 2823-2841. https://doi.org/10.1175/jcli-d-14-00300.1
15. Giorgi, F. (2019). Thirty Years of Regional Climate Modeling: Where Are We and Where Are We Going next? *Journal of Geophysical Research: Atmospheres*. https://doi.org/10.1029/2018jd030094
16. Grell, G. A., Schade, L., Knoche, R., Pfeiffer, A., & Egger, J. (2000). Nonhydrostatic climate simulations of precipitation over complex terrain. *Journal of Geophysical Research: Atmospheres, 105*(D24), 29595-29608. https://doi.org/10.1029/2000jd900445
17. Gu, H., Yu, Z., Peltier, W. R., & Wang, X. (2020). Sensitivity studies and comprehensive evaluation of RegCM4.6.1 high-resolution climate simulations over the Tibetan Plateau. *Climate Dynamics, 54*(7-8), 3781-3801. https://doi.org/10.1007/s00382-020-05205-6
18. Guo, Z., Fang, J., Sun, X., Tang, J., Yang, Y., & Tang, J. (2020). Decadal long convection-permitting regional climate simulations over eastern China: evaluation of diurnal cycle of precipitation. *Climate Dynamics, 54*(3), 1329-1349. https://doi.org/10.1007/s00382-019-05061-z
19. Guo, Z., Fang, J., Sun, X., Yang, Y., & Tang, J. (2019). Sensitivity of Summer Precipitation Simulation to Microphysics Parameterization Over Eastern China: Convection-Permitting Regional Climate

Simulation. *Journal of Geophysical Research: Atmospheres, 124*(16), 9183-9204. https://doi.org/10.1029/2019jd030295

20. Hersbach, H., Bell, B., Berrisford, P., Hirahara, S., Horányi, A., Muñoz-Sabater, J., Nicolas, J., Peubey, C., Radu, R., Schepers, D., Simmons, A., Soci, C., Abdalla, S., Abellan, X., Balsamo, G., Bechtold, P., Biavati, G., Bidlot, J., Bonavita, M., Chiara, G., Dahlgren, P., Dee, D., Diamantakis, M., Dragani, R., Flemming, J., Forbes, R., Fuentes, M., Geer, A., Haimberger, L., Healy, S., Hogan, R. J., Hólm, E., Janisková, M., Keeley, S., Laloyaux, P., Lopez, P., Lupu, C., Radnoti, G., Rosnay, P., Rozum, I., Vamborg, F., Villaume, S., & Thépaut, J. N. (2020). The ERA5 global reanalysis. *Quarterly Journal of the Royal Meteorological Society, 146*(730), 1999-2049. https://doi.org/10.1002/qj.3803
21. Iacono, M. J., Delamere, J. S., Mlawer, E. J., Shephard, M. W., Clough, S. A., & Collins, W. D. (2008). Radiative forcing by long-lived greenhouse gases: Calculations with the AER radiative transfer models. *Journal of Geophysical Research, 113*(D13). https://doi.org/10.1029/2008jd009944
22. Jacob, D., Petersen, J., Eggert, B., Alias, A., Christensen, O. B., Bouwer, L. M., Braun, A., Colette, A., Déqué, M., & Georgievski, G. (2014). EURO-CORDEX: new high-resolution climate change projections for European impact research. *Regional environmental change, 14*(2), 563-578. https://doi.org/10.1007/s10113-013-0499-2
23. Kang, S., Xu, Y., You, Q., Flügel, W.-A., Pepin, N., & Yao, T. (2010). Review of climate and cryospheric change in the Tibetan Plateau. *Environmental research letters, 5*(1). https://doi.org/10.1088/1748-9326/5/1/015101
24. Kuang, X., & Jiao, J. J. (2016). Review on climate change on the Tibetan Plateau during the last half century. *Journal of Geophysical Research: Atmospheres, 121*(8), 3979-4007. https://doi.org/10.1002/2015jd024728
25. Kukulies, J., Chen, D., & Wang, M. (2020). Temporal and spatial variations of convection, clouds and precipitation over the Tibetan Plateau from recent satellite observations. Part II: Precipitation climatology derived from global precipitation measurement mission. *International Journal of Climatology, 40*(11), 4858-4875. https://doi.org/10.1002/joc.6493
26. Li, P., Furtado, K., Zhou, T., Chen, H., & Li, J. (2021). Convection-permitting modelling improves simulated precipitation over the central and eastern Tibetan Plateau. *Quarterly Journal of the Royal Meteorological Society, 147*(734), 341-362. https://doi.org/10.1002/qj.3921
27. Li, P., Furtado, K., Zhou, T., Chen, H., Li, J., Guo, Z., & Xiao, C. (2020). The diurnal cycle of East Asian summer monsoon precipitation simulated by the Met Office Unified Model at convection-permitting scales. *Climate Dynamics, 55*(1), 131-151. https://doi.org/10.1007/s00382-018-4368-z
28. Li, X., Gao, Y., Pan, Y., & Xu, Y. (2018). Evaluation of near-surface wind speed simulations over the Tibetan Plateau from three dynamical downscalings based on WRF model. *Theoretical and Applied Climatology, 134*(3), 1399-1411. https://doi.org/10.1007/s00704-017-2353-9
29. Liang, X.-Z. (2004). Regional climate model simulation of summer precipitation diurnal cycle over the United States. *Geophysical Research Letters, 31*(24). https://doi.org/10.1029/2004gl021054

30. Lin, C., Chen, D., Yang, K., & Ou, T. (2018). Impact of model resolution on simulating the water vapor transport through the central Himalayas: implication for models' wet bias over the Tibetan Plateau. *Climate Dynamics, 51*(9-10), 3195-3207. https://doi.org/10.1007/s00382-018-4074-x
31. Liu, C., Ikeda, K., Rasmussen, R., Barlage, M., Newman, A. J., Prein, A. F., Chen, F., Chen, L., Clark, M., & Dai, A. (2017). Continental-scale convection-permitting modeling of the current and future climate of North America. *Climate Dynamics, 49*(1), 71-95. https://doi.org/10.1007/s00382-016-3327-9
32. Liu, X., & Chen, B. (2000). Climatic warming in the Tibetan Plateau during recent decades. *International Journal of Climatology: A Journal of the Royal Meteorological Society, 20*(14), 1729-1742. https://doi.org/10.1002/1097-0088(20001130)20:14<1729::AID-JOC556>3.0.CO;2-Y
33. Lu, D., & Yong, B. (2018). Evaluation and Hydrological Utility of the Latest GPM IMERG V5 and GSMaP V7 Precipitation Products over the Tibetan Plateau. *Remote Sensing, 10*(12). https://doi.org/10.3390/rs10122022
34. Lucas-Picher, P., Wulff-Nielsen, M., Christensen, J. H., Aðalgeirsdóttir, G., Mottram, R., & Simonsen, S. B. (2012). Very high resolution regional climate model simulations over Greenland: Identifying added value. *Journal of Geophysical Research: Atmospheres, 117*(D2). https://doi.org/10.1029/2011jd016267
35. Lv, M., Xu, Z., & Yang, Z. L. (2020). Cloud Resolving WRF Simulations of Precipitation and Soil Moisture Over the Central Tibetan Plateau: An Assessment of Various Physics Options. *Earth and Space Science, 7*(2). https://doi.org/10.1029/2019ea000865
36. Maussion, F., Scherer, D., Finkelnburg, R., Richters, J., Yang, W., & Yao, T. (2011). WRF simulation of a precipitation event over the Tibetan Plateau, China – an assessment using remote sensing and ground observations. *Hydrology and Earth System Sciences, 15*(6), 1795-1817. https://doi.org/10.5194/hess-15-1795-2011
37. Miura, H. (2007). An Upwind-Biased Conservative Advection Scheme for Spherical Hexagonal–Pentagonal Grids. *Monthly Weather Review, 135*(12), 4038-4044. https://doi.org/10.1175/2007mwr2101.1
38. Nakanishi, M., & Niino, H. (2006). An Improved Mellor–Yamada Level-3 Model: Its Numerical Stability and Application to a Regional Prediction of Advection Fog. *Boundary-Layer Meteorology, 119*(2), 397-407. https://doi.org/10.1007/s10546-005-9030-8
39. Ning, S., Song, F., Udmale, P., Jin, J., Thapa, B. R., & Ishidaira, H. (2017). Error Analysis and Evaluation of the Latest GSMap and IMERG Precipitation Products over Eastern China. *Advances in Meteorology, 2017*, 1-16. https://doi.org/10.1155/2017/1803492
40. Niu, G.-Y., Yang, Z.-L., Mitchell, K. E., Chen, F., Ek, M. B., Barlage, M., Kumar, A., Manning, K., Niyogi, D., Rosero, E., Tewari, M., & Xia, Y. (2011). The community Noah land surface model with multiparameterization options (Noah-MP): 1. Model description and evaluation with local-scale measurements. *Journal of Geophysical Research, 116*(D12). https://doi.org/10.1029/2010jd015139
41. Niu, X., Tang, J., Wang, S., Fu, C., & Chen, D. (2020). On the sensitivity of seasonal and diurnal precipitation to cumulus parameterization over CORDEX-EA-II. *Climate Dynamics, 54*(1), 373-

393. https://doi.org/10.1007/s00382-019-05010-w

42. Ou, T., Chen, D., Chen, X., Lin, C., Yang, K., Lai, H.-W., & Zhang, F. (2020). Simulation of summer precipitation diurnal cycles over the Tibetan Plateau at the gray-zone grid spacing for cumulus parameterization. *Climate Dynamics, 54*(7-8), 3525-3539. https://doi.org/10.1007/s00382-020-05181-x
43. Prein, A. F., Gobiet, A., Suklitsch, M., Truhetz, H., Awan, N. K., Keuler, K., & Georgievski, G. (2013). Added value of convection permitting seasonal simulations. *Climate Dynamics, 41*(9-10), 2655-2677. https://doi.org/10.1007/s00382-013-1744-6
44. Prein, A. F., Langhans, W., Fosser, G., Ferrone, A., Ban, N., Goergen, K., Keller, M., Tolle, M., Gutjahr, O., Feser, F., Brisson, E., Kollet, S., Schmidli, J., van Lipzig, N. P., & Leung, R. (2015, Jun). A review on regional convection-permitting climate modeling: Demonstrations, prospects, and challenges. *Rev Geophys, 53*(2), 323-361. https://doi.org/10.1002/2014RG000475
45. Qiu, J. (2008). China: the third pole. *Nature News, 454*(7203), 393-396. https://doi.org/10.1038/454393a
46. Rasmussen, R., Ikeda, K., Liu, C., Gochis, D., Clark, M., Dai, A., Gutmann, E., Dudhia, J., Chen, F., & Barlage, M. (2014). Climate change impacts on the water balance of the Colorado headwaters: High-resolution regional climate model simulations. *Journal of Hydrometeorology, 15*(3), 1091-1116. https://doi.org/10.1175/jhm-d-13-0118.1
47. Satoh, M., Tomita, H., Yashiro, H., Miura, H., Kodama, C., Seiki, T., Noda, A. T., Yamada, Y., Goto, D., & Sawada, M. (2014). The non-hydrostatic icosahedral atmospheric model: Description and development. *Progress in Earth and Planetary Science, 1*(1), 1-32. https://doi.org/10.1186/s40645-014-0018-1
48. Schlemmer, L., Hohenegger, C., Schmidli, J., Bretherton, C. S., & Schär, C. (2011). An Idealized Cloud-Resolving Framework for the Study of Midlatitude Diurnal Convection over Land. *Journal of the atmospheric sciences, 68*(5), 1041-1057. https://doi.org/10.1175/2010jas3640.1
49. Schwitalla, T., Warrach-Sagi, K., Wulfmeyer, V., & Resch, M. (2020). Near-global-scale high-resolution seasonal simulations with WRF-Noah-MP v.3.8.1. *Geoscientific Model Development, 13*(4), 1959-1974. https://doi.org/10.5194/gmd-13-1959-2020
50. Skamarock, W. C., Klemp, J. B., Dudhia, J., Gill, D. O., Liu, Z., Berner, J., Wang, W., Powers, J. G., Duda, M. G., & Barker, D. M. (2019). A description of the advanced research WRF model version 4. *National Center for Atmospheric Research: Boulder, CO, USA*, 145.
51. Sun, X., Xue, M., Brotzge, J., McPherson, R. A., Hu, X.-M., & Yang, X.-Q. (2016). An evaluation of dynamical downscaling of Central Plains summer precipitation using a WRF-based regional climate model at a convection-permitting 4 km resolution. *Journal of Geophysical Research: Atmospheres, 121*(23), 13,801-813,825. https://doi.org/10.1002/2016jd024796
52. Tang, J., Song, S., & Wu, J. (2010). Impacts of the spectral nudging technique on simulation of the East Asian summer monsoon. *Theoretical and Applied Climatology, 101*(1), 41-51. https://doi.org/10.1007/s00704-009-0202-1

53. Tang, J., Wang, S., Niu, X., Hui, P., Zong, P., & Wang, X. (2017). Impact of spectral nudging on regional climate simulation over CORDEX East Asia using WRF. *Climate Dynamics, 48*(7-8), 2339-2357. https://doi.org/10.1007/s00382-016-3208-2

54. Taraphdar, S., Pauluis, O. M., Xue, L., Liu, C., Rasmussen, R., Ajayamohan, R. S., Tessendorf, S., Jing, X., Chen, S., & Grabowski, W. W. (2021). WRF Gray-Zone Simulations of Precipitation Over the Middle-East and the UAE: Impacts of Physical Parameterizations and Resolution. *Journal of Geophysical Research: Atmospheres, 126*(10). https://doi.org/10.1029/2021jd034648

55. Taylor, K. E. (2001). Summarizing multiple aspects of model performance in a single diagram. *Journal of Geophysical Research: Atmospheres, 106*(D7), 7183-7192. https://doi.org/10.1029/2000jd900719

56. Thompson, G., Field, P. R., Rasmussen, R. M., & Hall, W. D. (2008). Explicit forecasts of winter precipitation using an improved bulk microphysics scheme. Part II: Implementation of a new snow parameterization. *Monthly Weather Review, 136*(12), 5095-5115. https://doi.org/10.1175/2008mwr2387.1

57. Tian, Y., Peters-Lidard, C. D., Adler, R. F., Kubota, T., & Ushio, T. (2010). Evaluation of GSMaP Precipitation Estimates over the Contiguous United States. *Journal of Hydrometeorology, 11*(2), 566-574. https://doi.org/10.1175/2009jhm1190.1

58. von Storch, H., Langenberg, H., & Feser, F. (2000). A spectral nudging technique for dynamical downscaling purposes. *Monthly Weather Review, 128*(10), 3664-3673. https://doi.org/10.1175/1520-0493(2000)128<3664:ASNTFD>2.0.CO;2

59. Wang, X., Chen, D., Pang, G., Anwar, S. A., Ou, T., & Yang, M. (2021). Effects of cumulus parameterization and land-surface hydrology schemes on Tibetan Plateau climate simulation during the wet season: insights from the RegCM4 model. *Climate Dynamics*. https://doi.org/10.1007/s00382-021-05781-1

60. Wang, Y., Wang, L., Li, X., & Chen, D. (2018). Temporal and spatial changes in estimated near-surface air temperature lapse rates on Tibetan Plateau. *International Journal of Climatology, 38*(7), 2907-2921. https://doi.org/10.1002/joc.5471

61. Warrach-Sagi, K., Schwitalla, T., Wulfmeyer, V., & Bauer, H.-S. (2013). Evaluation of a climate simulation in Europe based on the WRF–NOAH model system: precipitation in Germany. *Climate Dynamics, 41*(3-4), 755-774. https://doi.org/10.1007/s00382-013-1727-7

62. Weisman, M. L., Skamarock, W. C., & Klemp, J. B. (1997). The resolution dependence of explicitly modeled convective systems. *Monthly Weather Review, 125*(4), 527-548. https://doi.org/10.1175/1520-0493(1997)125<0527:TRDOEM>2.0.CO;2

63. Wu, G., Liu, Y., Zhang, Q., Duan, A., Wang, T., Wan, R., Liu, X., Li, W., Wang, Z., & Liang, X. (2007). The influence of mechanical and thermal forcing by the Tibetan Plateau on Asian climate. *Journal of Hydrometeorology, 8*(4), 770-789. https://doi.org/10.1175/jhm609.1

64. XIAO, L., GAO, Y., CHEN, F., XU, J., LI, K., LI, X., & JIANG, Y. (2016). Dynamic downscaling simulation of extreme temperature indices over the Qinghai-Xizang plateau. *Plateau Meteorology, 35*(3), 574-

589. https://doi.org/10.7522/j.issn.1000-0534.2016.00039

65. Xu, J., Koldunov, N., Remedio, A. R. C., Sein, D. V., Zhi, X., Jiang, X., Xu, M., Zhu, X., Fraedrich, K., & Jacob, D. (2018). On the role of horizontal resolution over the Tibetan Plateau in the REMO regional climate model. *Climate Dynamics, 51*(11-12), 4525-4542. https://doi.org/10.1007/s00382-018-4085-7
66. Xu, Z., Mahmood, R., Yang, Z. L., Fu, C., & Su, H. (2015). Investigating diurnal and seasonal climatic response to land use and land cover change over monsoon Asia with the Community Earth System Model. *Journal of Geophysical Research: Atmospheres, 120*(3), 1137-1152. https://doi.org/10.1002/2014jd022479
67. Xu, Z. X., Gong, T. L., & Li, J. Y. (2008). Decadal trend of climate in the Tibetan Plateau—regional temperature and precipitation. *Hydrological Processes, 22*(16), 3056-3065. https://doi.org/10.1002/hyp.6892
68. Yao, T., Xue, Y., Chen, D., Chen, F., Thompson, L., Cui, P., Koike, T., Lau, W. K. M., Lettenmaier, D., Mosbrugger, V., Zhang, R., Xu, B., Dozier, J., Gillespie, T., Gu, Y., Kang, S., Piao, S., Sugimoto, S., Ueno, K., Wang, L., Wang, W., Zhang, F., Sheng, Y., Guo, W., Ailikun, Yang, X., Ma, Y., Shen, S. S. P., Su, Z., Chen, F., Liang, S., Liu, Y., Singh, V. P., Yang, K., Yang, D., Zhao, X., Qian, Y., Zhang, Y., & Li, Q. (2019). Recent Third Pole's Rapid Warming Accompanies Cryospheric Melt and Water Cycle Intensification and Interactions between Monsoon and Environment: Multidisciplinary Approach with Observations, Modeling, and Analysis. *Bulletin of the American Meteorological Society, 100*(3), 423-444. https://doi.org/10.1175/bams-d-17-0057.1
69. Yeh, T.-C. (1957). The wind structure and heat balance in the lower troposphere over the Tibetan Plateau and its surroundings. *Acta. Meteor. Sinica, 28*, 108-121.
70. Yun, Y., Liu, C., Luo, Y., Liang, X., Huang, L., Chen, F., & Rasmmusen, R. (2020). Convection-permitting regional climate simulation of warm-season precipitation over Eastern China. *Climate Dynamics, 54*(3), 1469-1489. https://doi.org/10.1007/s00382-019-05070-y
71. Zhang, Y., & Chen, H. (2016). Comparing CAM5 and Superparameterized CAM5 Simulations of Summer Precipitation Characteristics over Continental East Asia: Mean State, Frequency–Intensity Relationship, Diurnal Cycle, and Influencing Factors. *Journal of Climate, 29*(3), 1067-1089. https://doi.org/10.1175/jcli-d-15-0342.1
72. Zhou, X., Yang, K., Ouyang, L., Wang, Y., Jiang, Y., Li, X., Chen, D., & Prein, A. (2021). Added value of kilometer-scale modeling over the third pole region: a CORDEX-CPTP pilot study. *Climate Dynamics*. https://doi.org/10.1007/s00382-021-05653-8
73. Zhu, L., Huang, G., Fan, G., Qu, X., Zhao, G., & Hua, W. (2017). Evolution of surface sensible heat over the Tibetan Plateau under the recent global warming hiatus. *Advances in Atmospheric Sciences, 34*(10), 1249-1262. https://doi.org/10.1007/s00376-017-6298-9

Figures

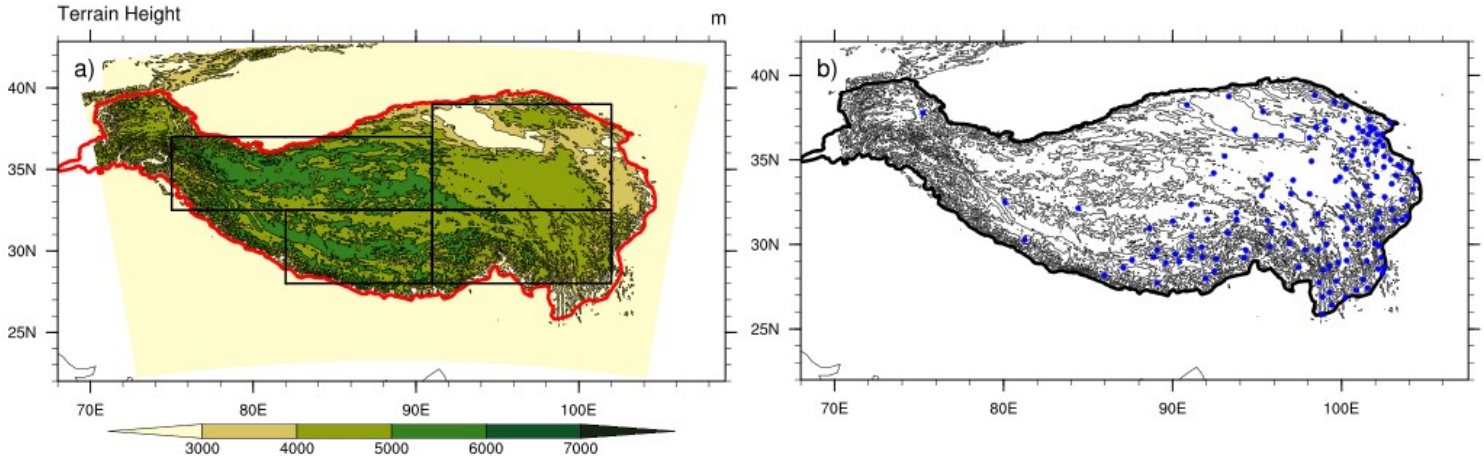

Figure 1

The simulation domain (yellow shading) with the TP framed with red lines and four sub-regions framed with black lines (a), and the locations of the meteorological stations over the TP (b)

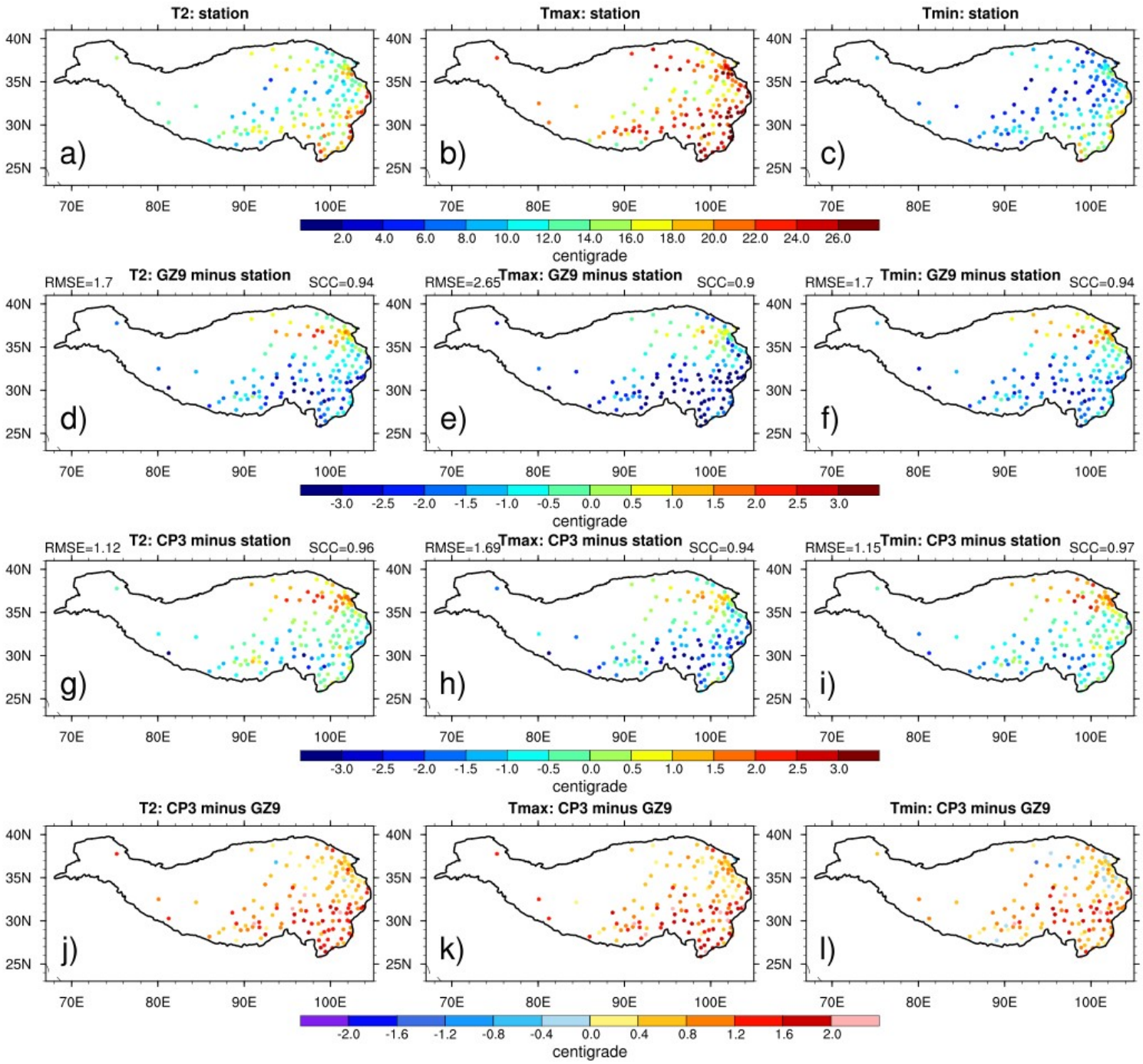

Figure 2

The 11-year averaged (2009-2019) summer mean T2m, Tmax, and Tmin from the in-situ observations (a, b, c), the biases in GZ9 (d, e, f), the bias in CP3 (g, h, i), and the difference between CP3 and GZ9 (j, k, l)

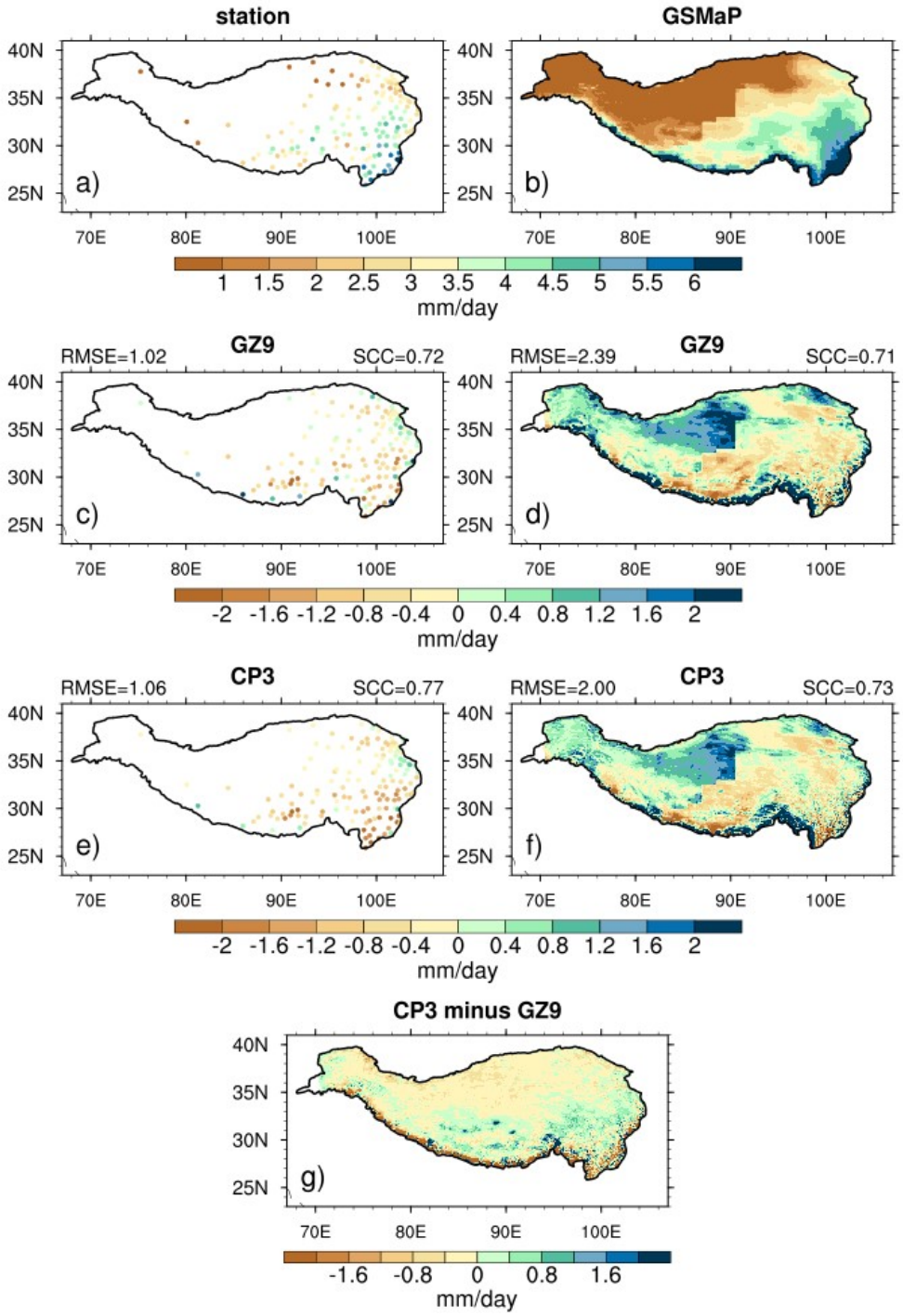

Figure 3

11-year averaged summer precipitation from the station observations (a), the GSMaP satellite dataset (b), the difference between GZ9 and station observations as well as the GSMaP dataset (c, d), the difference between CP3 and station observations as well as the GSMaP dataset (e, f), and the difference between CP3 and GZ9 (g)

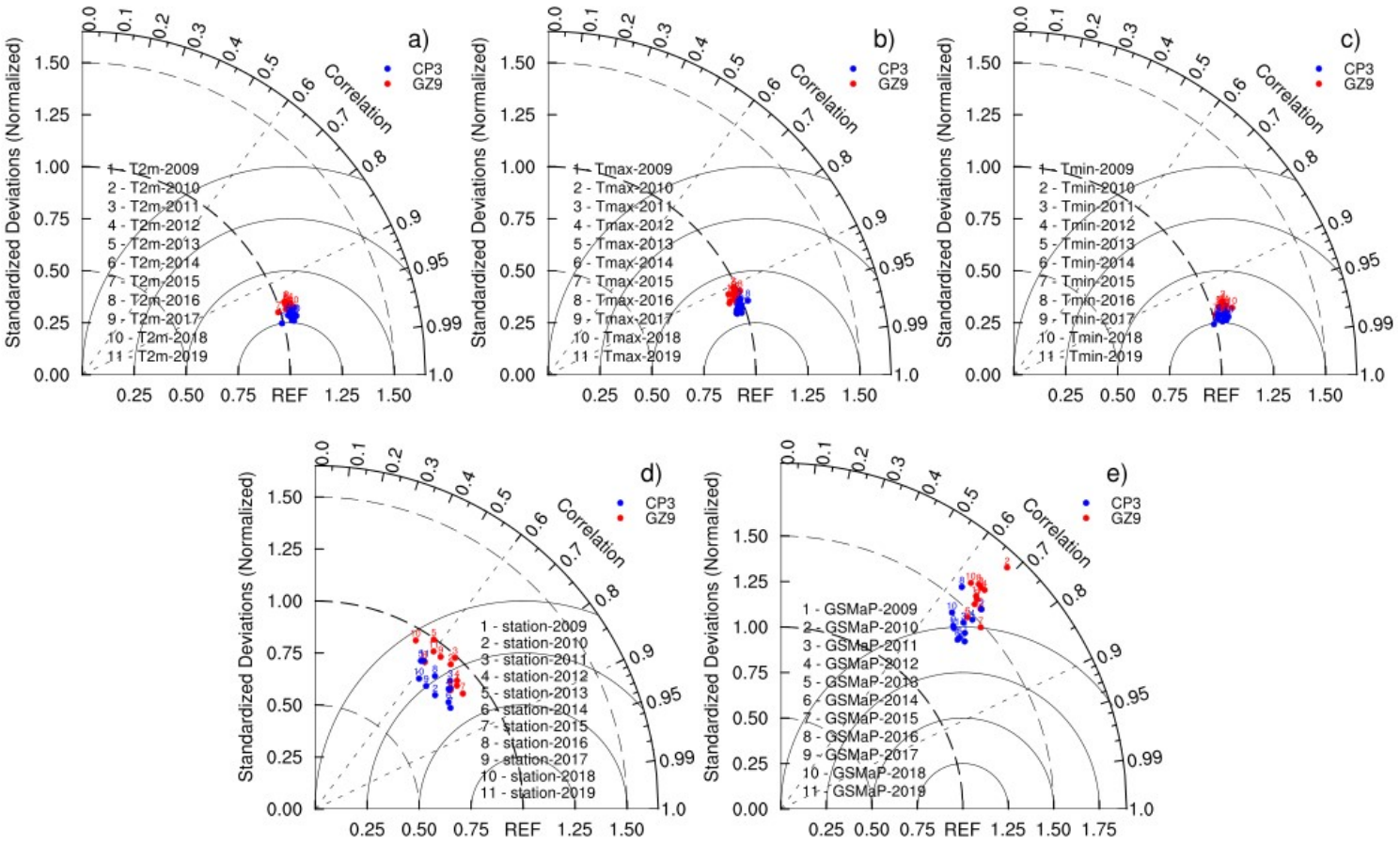

Figure 4

Taylor diagrams for WRF simulated summer T2m (a), Tmax (b), Tmin (c), precipitation (d) compared with station observations, as well as summer precipitation compared with the GSMaP dataset (e) from 2009 to 2019

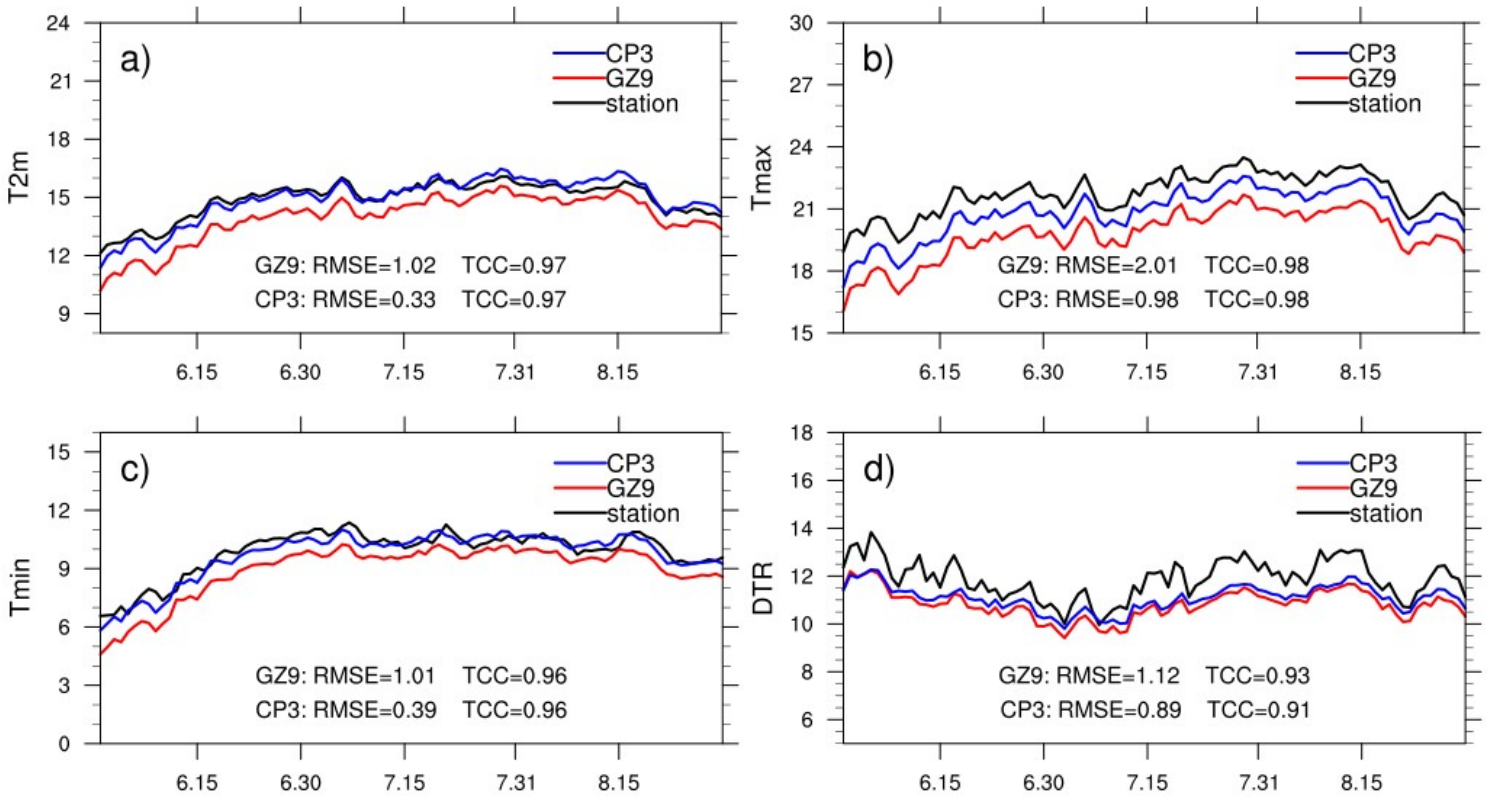

Figure 5

11-year averaged daily variations of regional mean T2m (a), Tmax (b), Tmin (c), and DTR (d) from the in-situ observations and the simulations of CP3 and GZ9

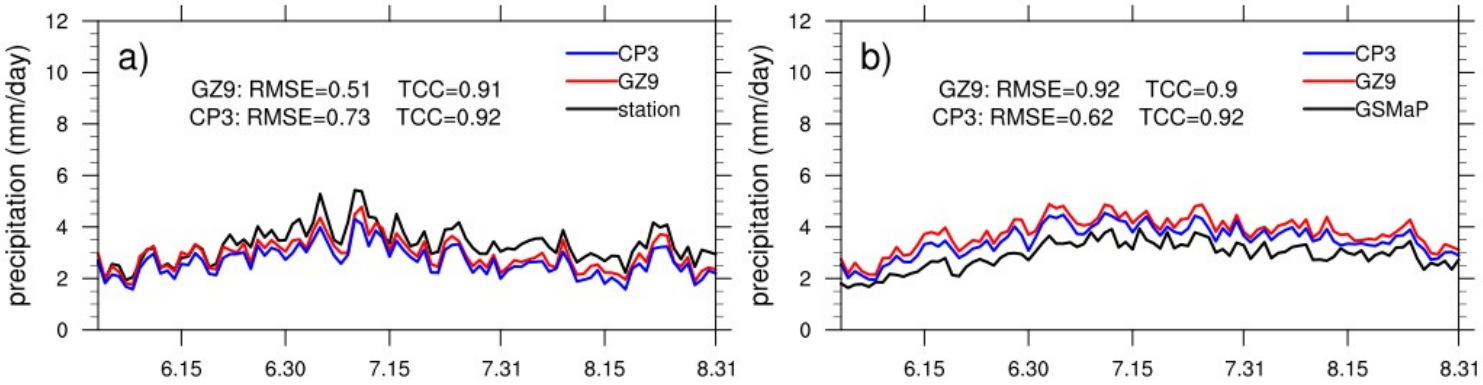

Figure 6

11-year averaged daily variation of regional mean precipitation over the TP from the station observation (a) and the GSMaP dataset (b) accompanied with that in the two WRF experiments

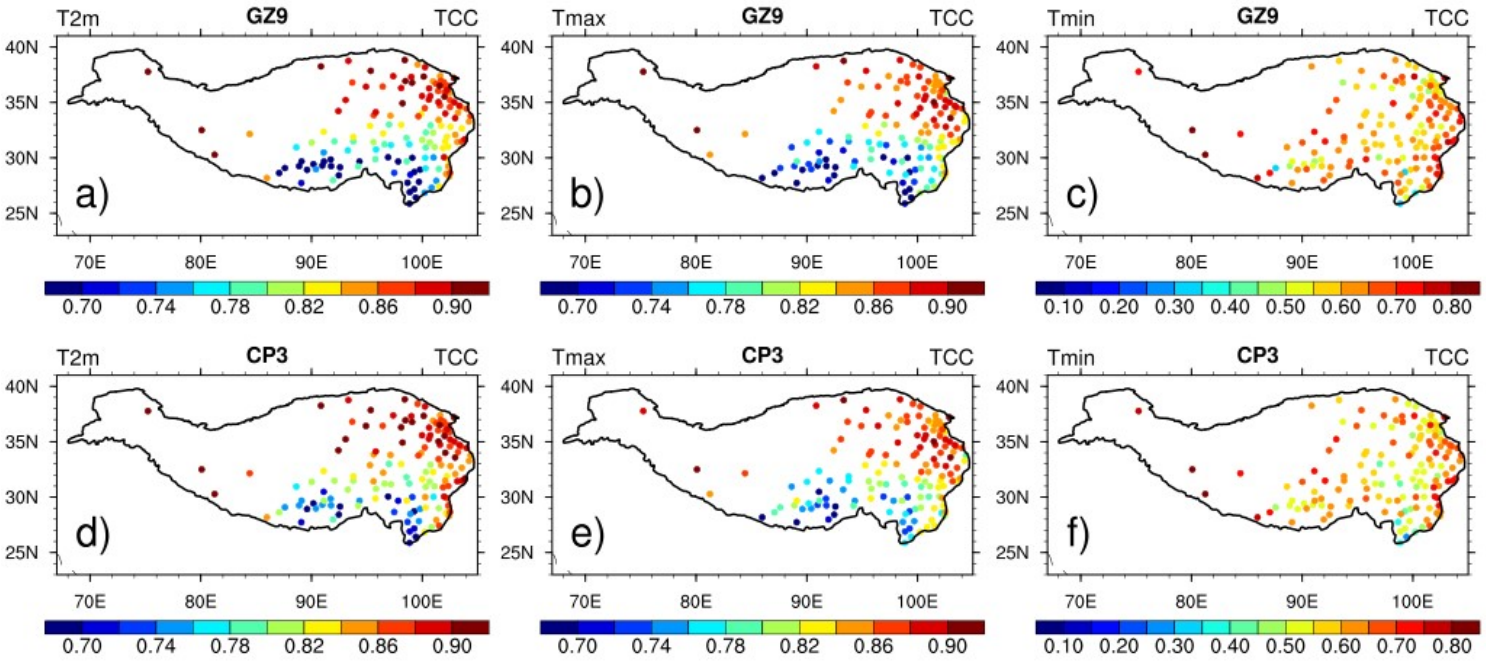

Figure 7

The spatial distributions of TCCs for the simulated summer T2m, Tmax, and Tmin in GZ9 (a, b, c) and CP3 (d, e, f)

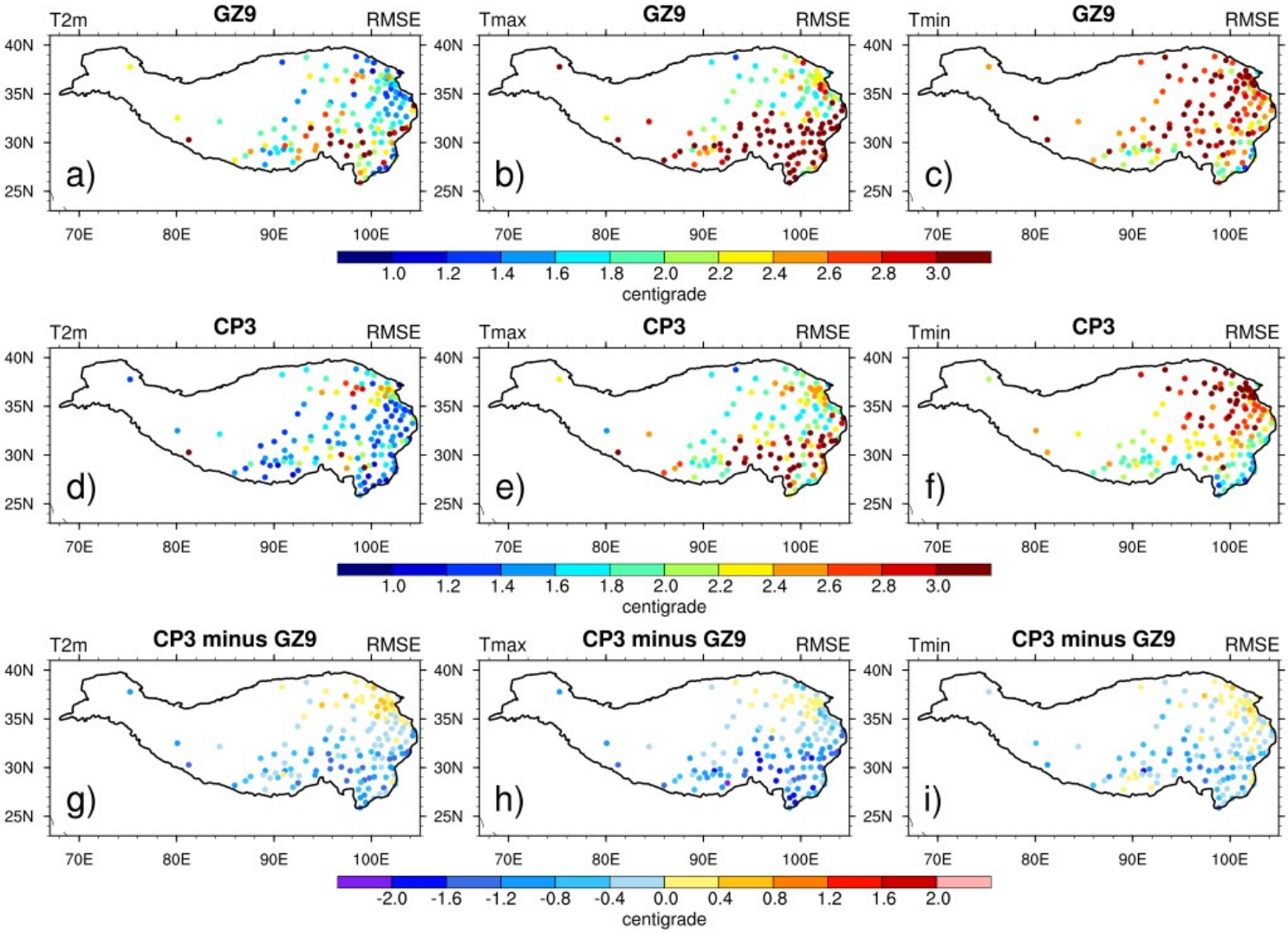

Figure 8

The spatial distributions of RMSEs for the simulated summer T2m, Tmax, and Tmin in GZ9 (a, b, c) and CP3 (d, e, f), as well as the difference between CP3 and GZ9 (g, h, i)

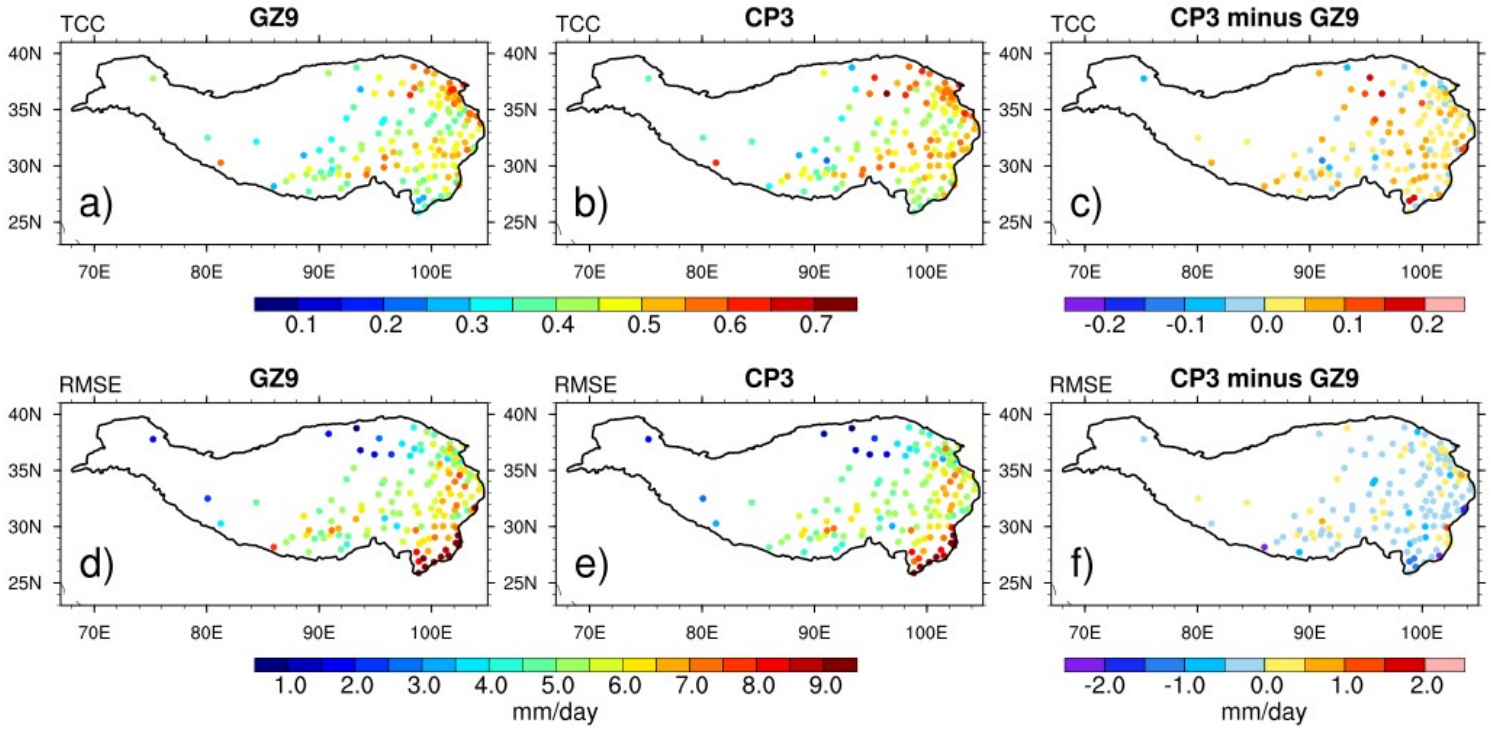

Figure 9

The spatial distribution of TCC and RMSE for the simulated precipitation in GZ9 (a and d), CP3 (b and e) and the difference between CP3 and GZ9 (c and f)

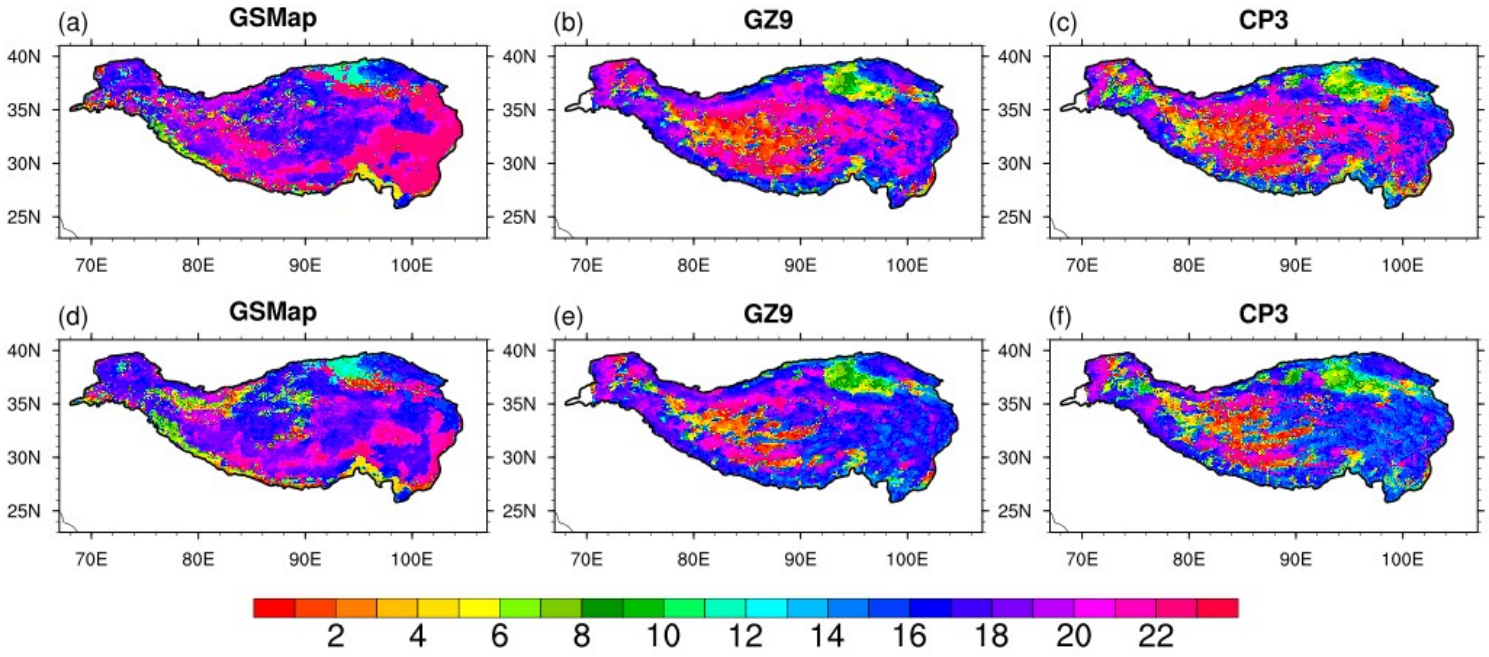

Figure 10

11-year averaged occurrence time of maximum PA and PF in the observation (a and d) and the WRF experiments (GZ9: b and c; CP3: e and f)

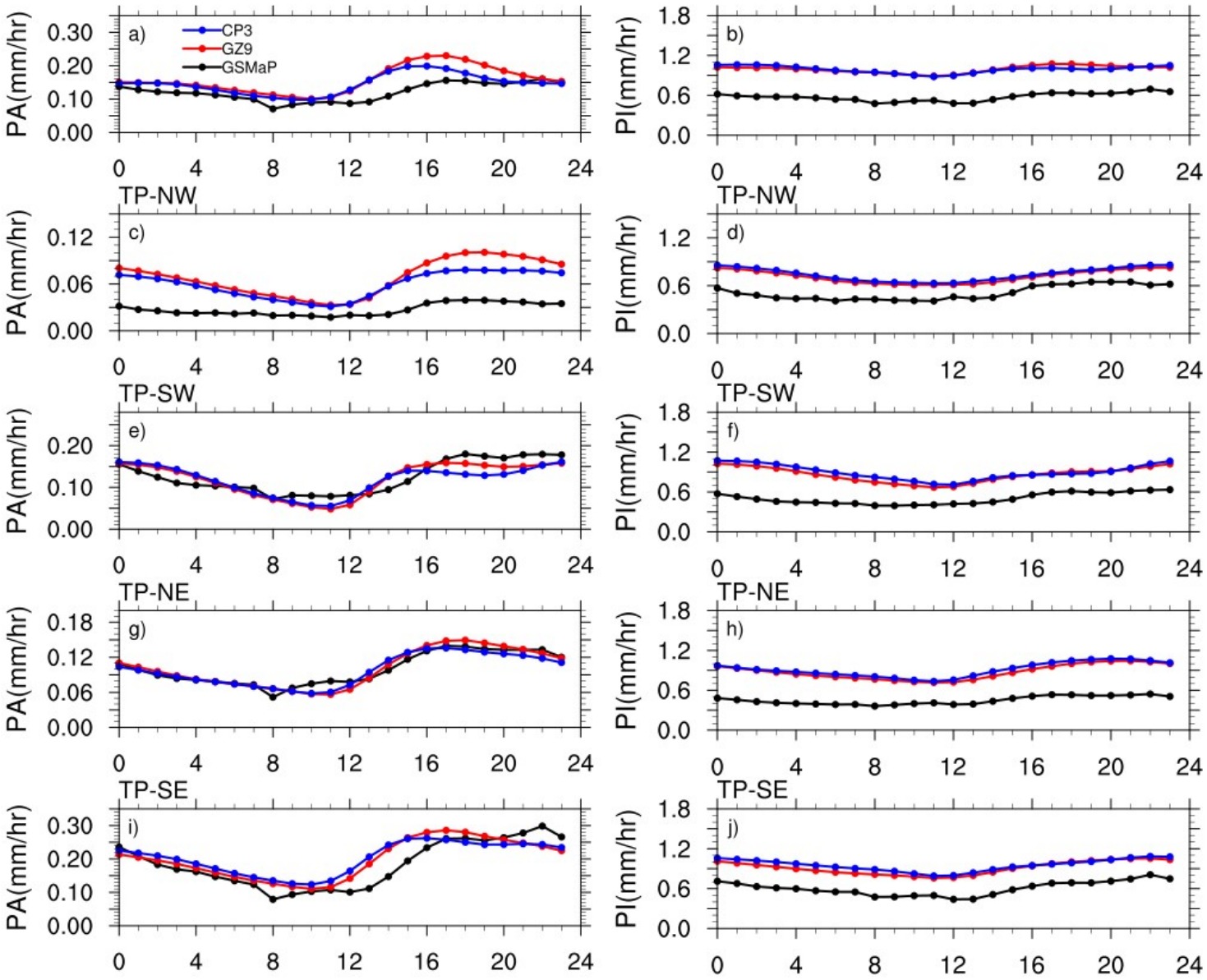

Figure 11

11-year averaged regional mean diurnal cycle of precipitation amount (PA) and precipitation intensity (PI) over the whole TP (a and b) and four sub-regions shown in Fig. 1: TP-NW (c and d), TP-SW (e and f), TP-NE (g and h) and TP-SE (i and j)

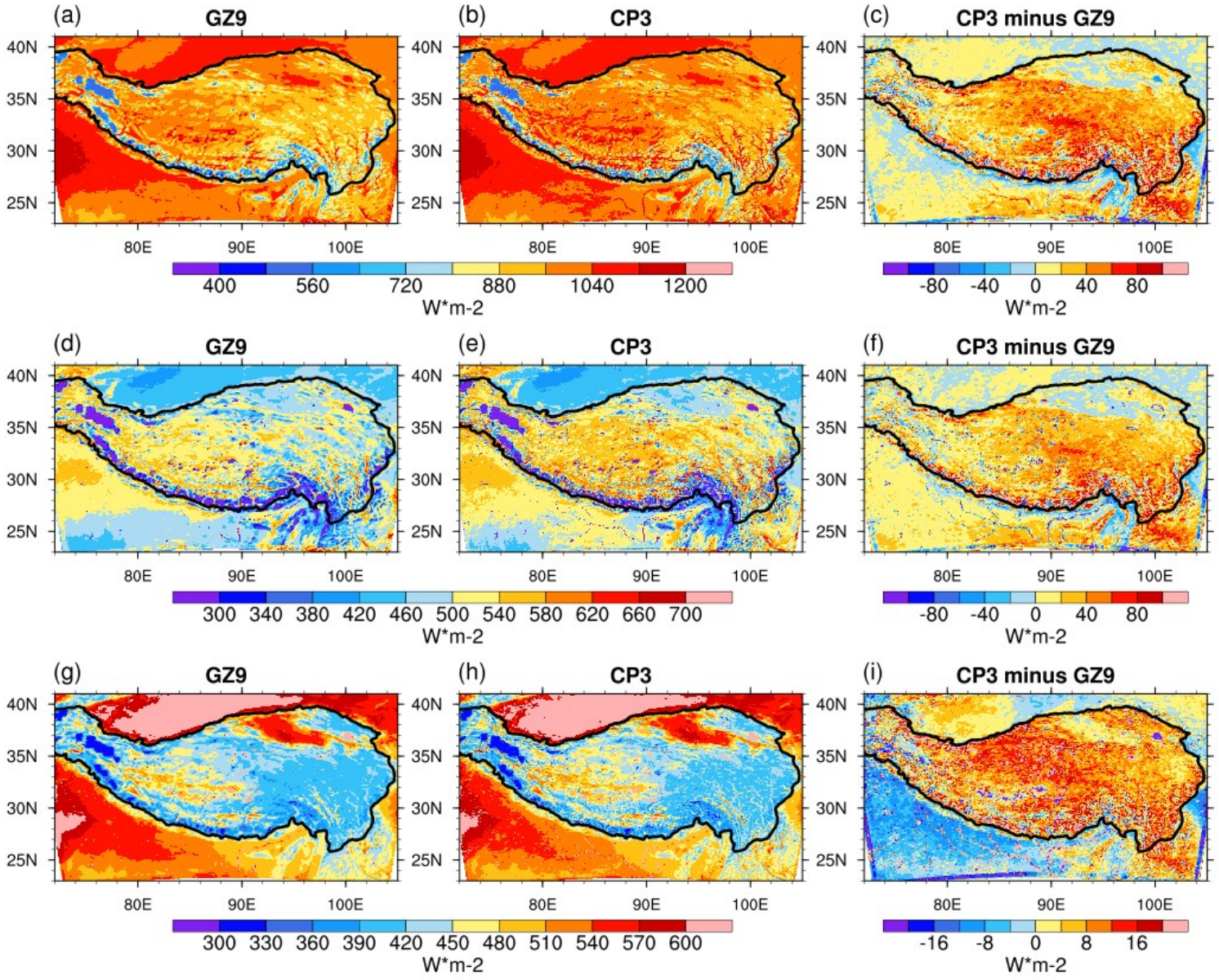

Figure 12

11-year averaged radiative energy, non-radiative energy and the energy balance at 14:00 LST for GZ9 (a, d and g), CP3 (b, e and h), and the difference between CP3 and GZ9 (c, f and i). In the first row, received radiative energy (SW↓-SW↑+LW↓) is represented with positive values. In the second row, non-radiative energy loss (SH+LH+GHF) is represented with positive values. In the third row, net energy obtained (SW↓-SW↑+LW↓-SH-LH-GHF) is represented with positive values

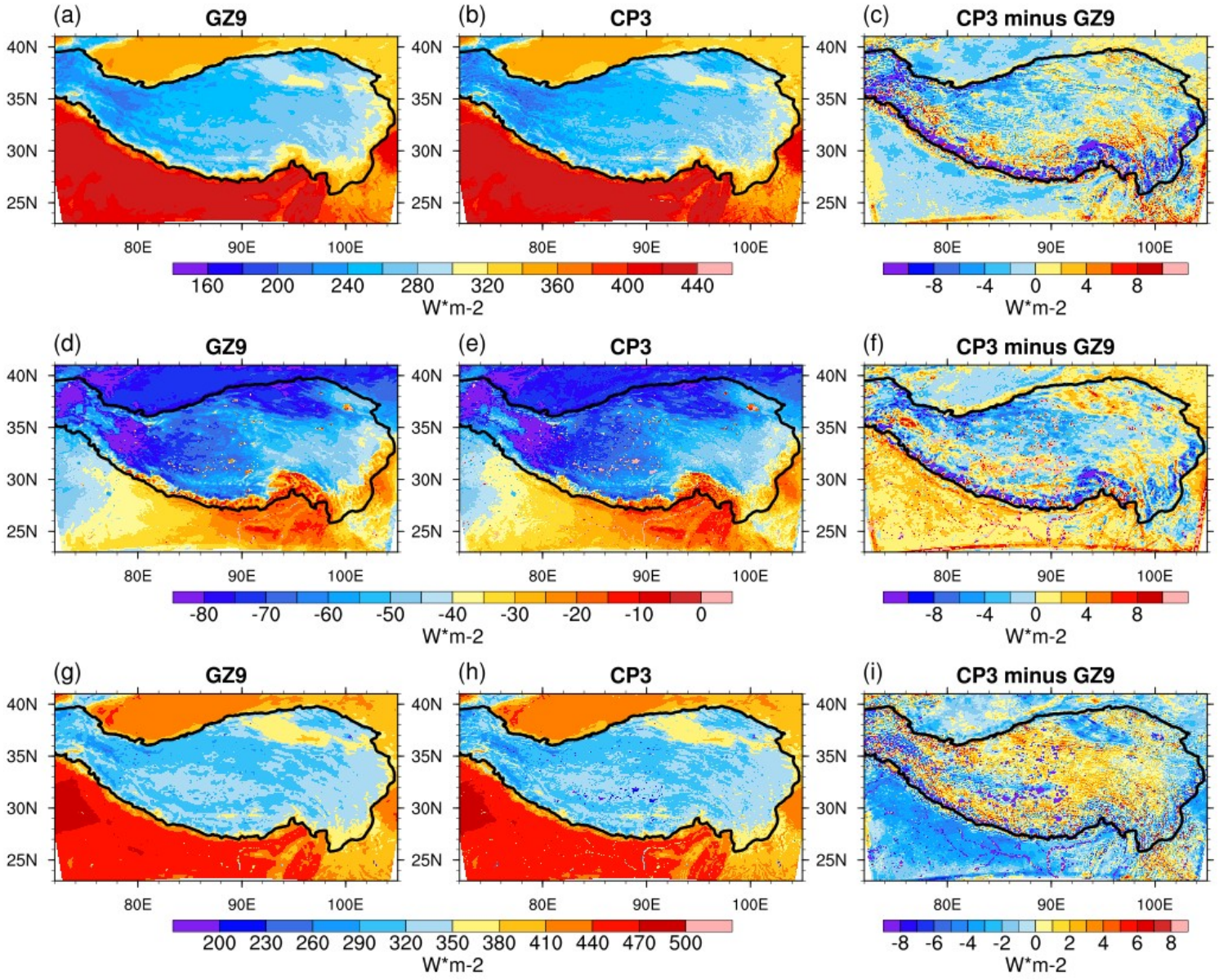

Figure 13

Same as Figure 12, but at 02:00 LST

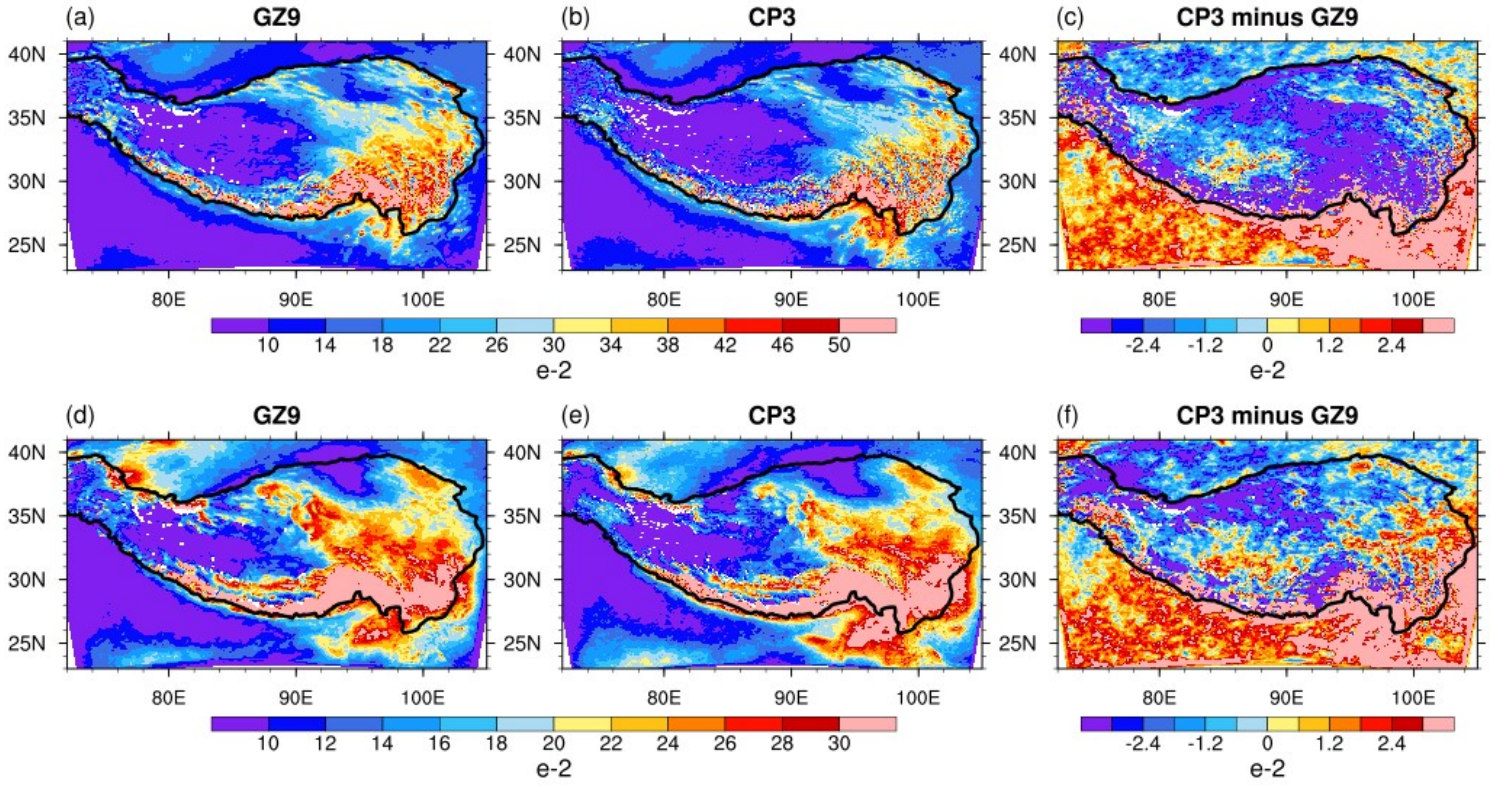

Figure 14

11-year averaged cloud fraction at 500hPa at 14:00 LST and 02:00 LST for GZ9 (a, d), CP3 (b, e), and the difference between CP3 and GZ9 (c, f)

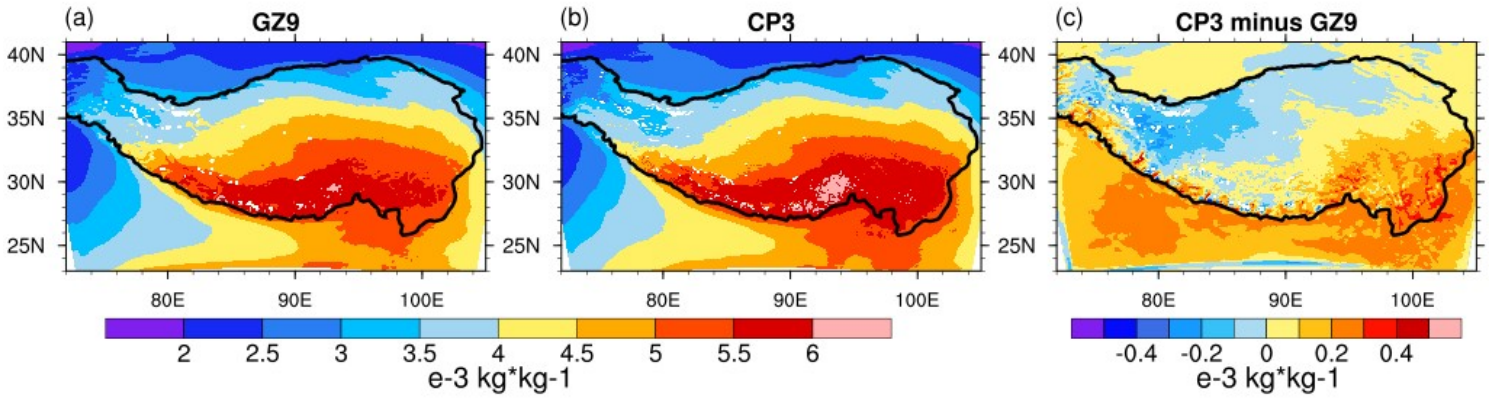

Figure 15

11-year averaged water vapor mixing ratio at 500hPa in GZ9 (a), CP3 (b) and the difference between them (c)